04

Advanced Optical Metrology

Roughness

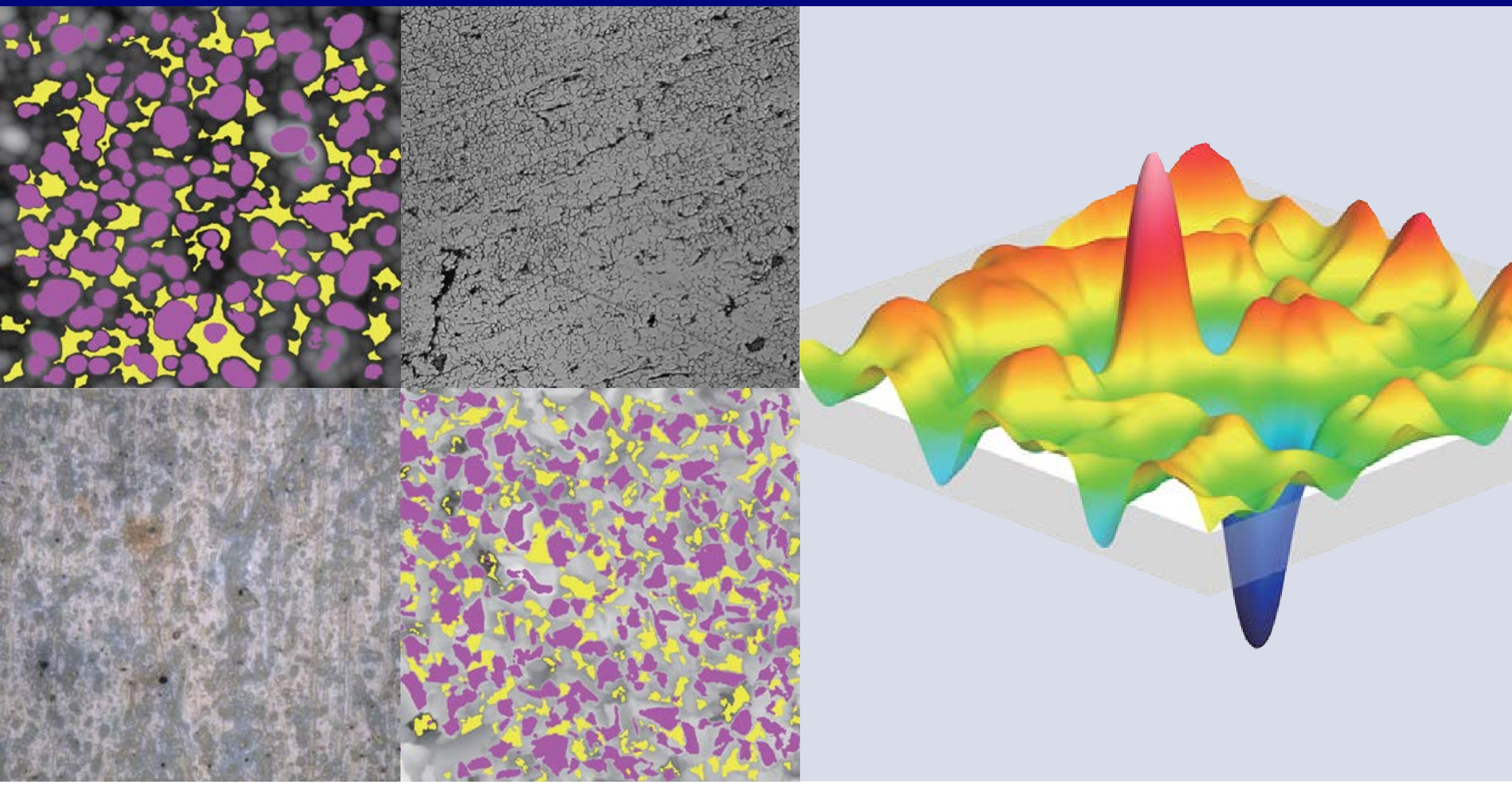

OLYMPUS

WILEY

Contents

Imprint

Boschstr. 12, 69469 Weinheim, Germany
Email: info@wiley-vch.de
Editor-in-Chief: Dr. Christina Poggel

Surface Roughness

Lawrence A. Renna

Surface roughness has critical implications for the properties and function of materials including, wettability, friction resistance, optical properties, anti-scaling performance, corrosion resistance, sensor activity, and electronic properties, to name a few. Thus, using surface metrology to characterize surface roughness provides important information in describing material morphology. Scanning electron microscope (SEM) and scanning probe techniques such as profilometry and atomic force microscopy (AFM) are the more traditional methods for investigating surface roughness. Surface roughness analysis by SEM usually requires additional sample preparation (e.g., gold sputtering), and SEM images typically cannot quantify surface texture characteristics or precise morphologies over a large surface area. AFM can measure very small surface roughness features; however, it is often difficult to perform on very soft or sticky surfaces, and cannot characterize surfaces with small and large surface features. [1] Thus arises optical metrology, specifically laser scanning confocal microscopy (LSCM) to address many of the needs of surface metrology.

LASER SCANNING CONFOCAL MICROSCOPY

LSCM is a topological optical microscopy technique that can create a bright image of the specimen's in-focus region while causing all out-of-focus areas to appear dark. One of the major limitations of traditional optical microscopy is the narrow depth of field. LSCM can take a series of optical sections, at different optical planes, to assemble a "through-focus" image. This feature endows LSCM with a virtually infinite depth of field. [2]

Two different modes of LSCM operation are typically used to characterize material structures. They are fluorescence-mode LSCM and reflectance-mode LSCM. Fluorescence-mode uses the excitation of fluorophores to generate image contrast, whereas reflectance-mode is used to characterize the surface texture or roughness of material surfaces. [1] In reflectance mode, a 405 nm laser is typically used because it provides the smallest probe size. Moreover, highly tuned optics provides extremely high, sub-micron resolution. [3]

In scanning probe techniques, roughness measurements are generally made along a straight line by scanning the sample's surface with a probe. LSCM instruments can perform a line-scan such that the instrument measures the surface features along a defined line in any orientation, providing the same roughness features as scanning probe methods. However, LSCM can also measure the surface features of the entire area of a sample, which provides a more representative view of the overall surface. [3]

The quantification of surface features results in surface parameters, and are discussed in the next section. Surface parameters are characterized by profile methods and areal methods. Profile methods were derived for conventional stylus probe measurements, but can be easily calculated from LSCM measurements. Areal methods can characterize the entire surface rather than just a line across the surface and are one of the main benefits of using LSCM. [1]

Profile Methods. The primary profile curve is obtained by applying a low-pass filter to the measured primary profile. The surface texture parameter calculated from the primary profile is referred to as the primary profile parameter (P-parameter). The roughness profile can be derived from the primary profile by applying a high-pass filter to remove the long wave components of the profile. The surface texture parameter calculated from the roughness profile is referred to as the roughness profile parameter (R-parameter). Lastly, the waviness profile is derived from the primary profile by applying a larger high-pass filter to remove the long-wave components greater than the waviness components, followed by a cutoff filter to remove

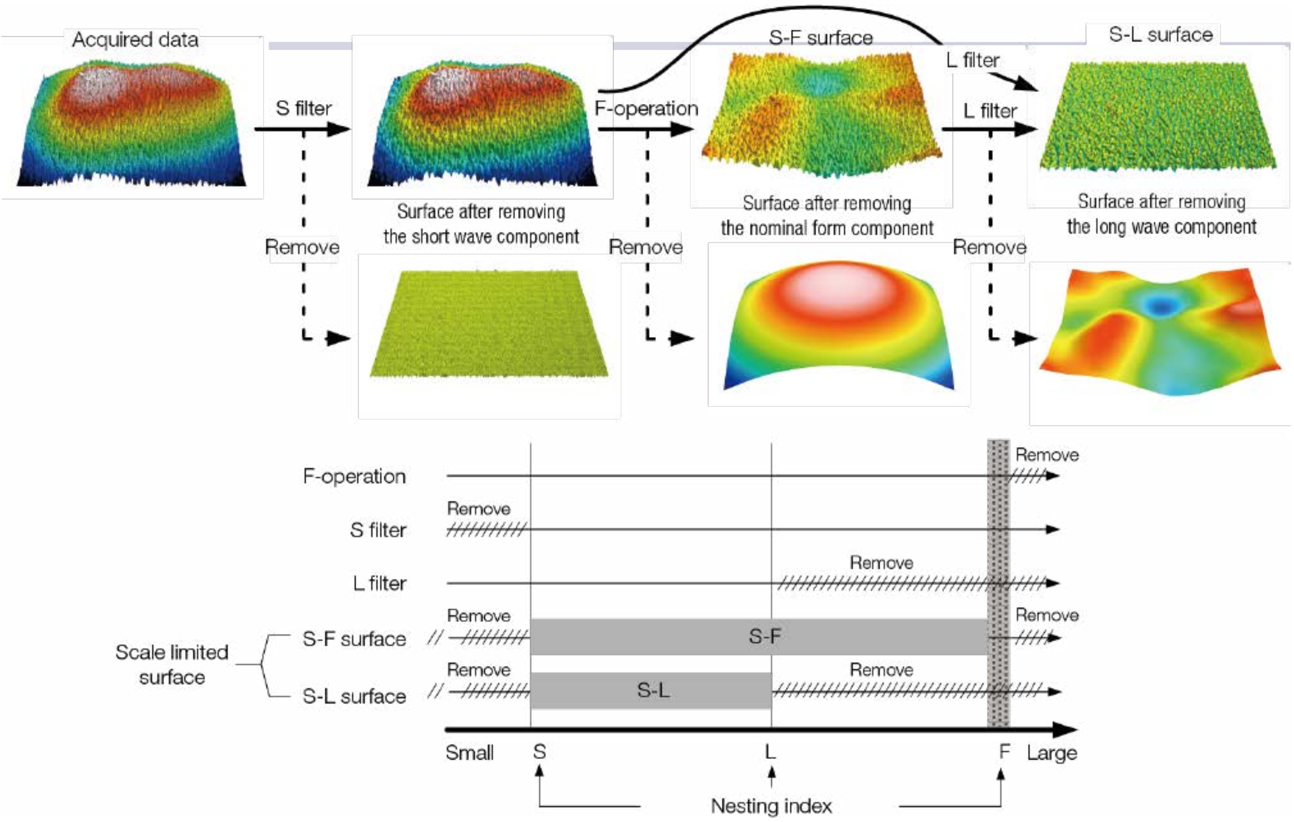

Figure 1: Top, an example of the application of areal filters to a surface obtained by confocal microscopy showing the eliminated and resulting surfaces from the application of the filters. Bottom, conceptual drawing of the areal methods of analysis, displaying filters and their respective nesting indices, and the length-scale information contained within different calculated surfaces. Reproduced with permission from Ref. [4].

the roughness components from the profile. The surface texture parameter calculated from the waviness profile is referred to as the waviness profile parameter (W-parameter). [4]

Areal Methods. Filters are also used to calculate new surfaces (called areal filters), which display the features of a surface at different length/height scales. The filters effectively separate the long and/or short wave components contained in the scale-limited surfaces. According to function, three types of filters are defined: the S filter eliminates the small wavelength components, the L filter that eliminates the large wavelength components, and the F operation, which removes specific forms (e.g., spherical or cylindrical features). The value representing the threshold wavelength for areal filters is called the nesting index and is equivalent to cutoff values used in profile methods. [4] Combinations of filters can be utilized to calculate new surfaces that display features at different length scales. The S-F surface is obtained by applying a Gaussian low-pass S filter to remove noise and keep the primary surface followed by applying an F operator to remove the form. The S-F surface displays the texture of the material's surface. By applying a Gaussian high-pass L filter to the S-F surface, the waviness is filtered out and leaves the S-L surface. The S-L surface displays the surface roughness of the analyzed material. [5] An example application of the S filter, L filter, and F operation, and the resulting surfaces are shown in **Figure 1**. Moreover, **Figure 1** also displays a conceptual drawing of areal methods displaying the filters and their respective nesting indices, and the length-scale information contained within different calculated surfaces. [4]

SURFACE ROUGHNESS PARAMETERS

Superficial irregularities (roughness and undulation), dents, parallel grooves, and other characteristic surface features are collectively called "surface textures." Converting these surface characteristics into numerical measurements is referred to as surface texture parameters. Surface texture parameters are roughly categorized into the profile methods and the areal methods. [4]

A variety of parameters can characterize surface roughness. Areal/field parameters are used to describe the entire measured surface of the sample, whereas feature parameters only consider select points, lines, or areas of the sample. [6] Surface roughness parameters provide more information, and their determination is uniquely enabled by confocal microscopy. ISO 25178 categorizes the 3-D

Table 1: ISO 25178 roughness parameters. Adapted from Ref. [7].

Group	Parameters	Notes
Height Parameters	Sa, Sq, Ssk, Sku, Sp, Sv, Sz	Amplitude methods, defined for the defined area
Functional Parameters 1	Smr, Smc, Sk, Spk, Svk	Areal material ratio as a function of the scale-limited stratified functional surface
Functional Parameters 2	Svq, Spq, Smq	Areal material probability curve, with the areal material area ratio expressed as a Gaussian probability
Volume Parameters	Vm, Vv, Vmp, Vmc, Vvc, Vvv	
Functional Parameters 3	Svs, Srel, Svfc, Safc	Fractal cross-scale descriptive methods
Hybrid Parameters	Sdq, Sdr	Surface envelope and gradients
Spatial Parameters	Sal, Str	Autocorrelation functions
Other Parameters	Std	Texture direction

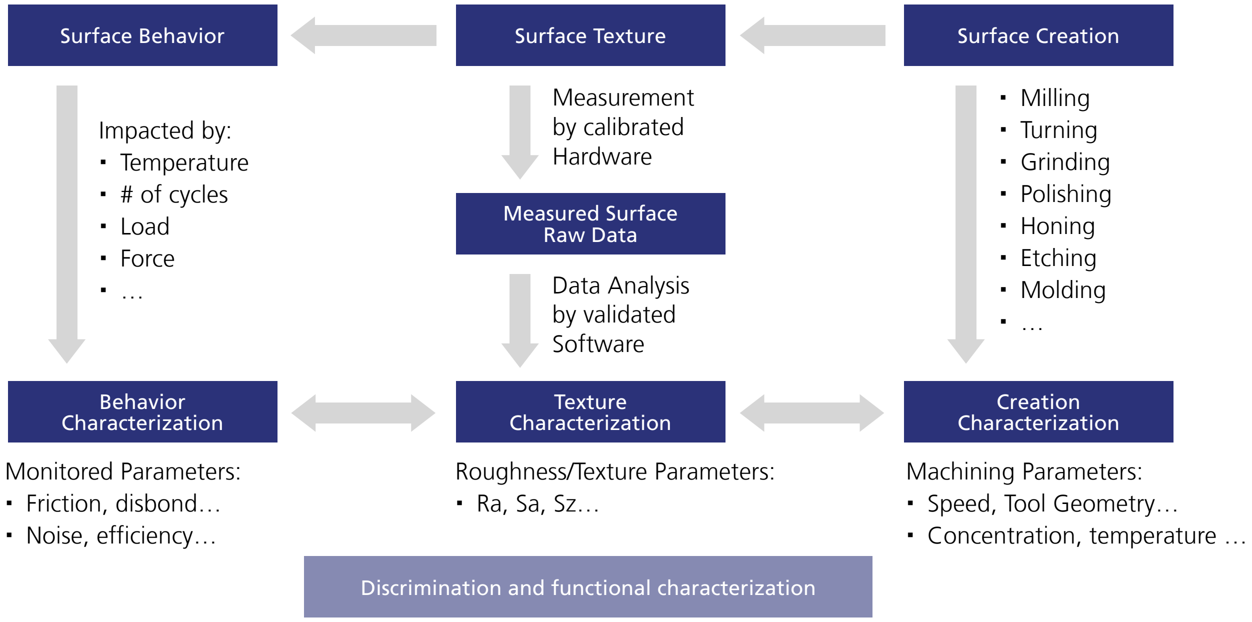

Figure X: Surface Metrology and Scales – Why and how?

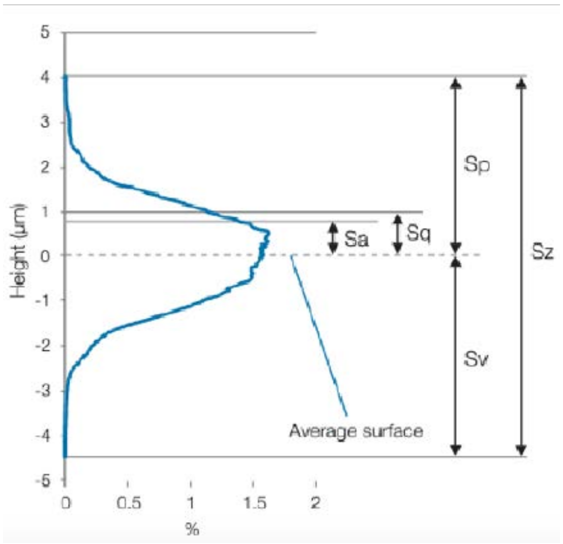

Figure 2: Height distribution obtained from LSCM showing the selected areal height parameters. Reproduced with permission from Ref. [4].

surface parameters into six groups as shown in **Table 1**. [7] Surface parameters have the symbol S, and volume parameters have the symbol V. The selected area and filtering are not defined by the parameter designation; therefore, the filtering conditions should be stated when reporting a surface parameter. [6]

The areal surface height parameters are commonly used to describe the height distribution or the unevenness of a surface, and select parameters are presented in **Table 2**. Height parameters are calculated using the distribution of height information from the measurement. [6] Therefore, lateral features are not captured by these parameters, but can be described by other parameters in **Table 1**. [8] An example height histogram obtained by confocal microscopy is shown in **Figure 2** and shows the relationship between the selected areal height parameters and the height distribution. [4]

Table 2: Selected areal surface unevenness height parameters. Adapted from Ref. [8].

Parameter	Definition
Sq	Root mean square height is the standard deviation of the height distribution, or RMS surface roughness
Sp	Maximum peak height is the height between the highest peak and the mean plane
Sv	Maximum pit height is the depth between the mean plane and the deepest valley
Sz	Maximum height is the height between the highest peak and the deepest valley
Sa	Arithmetical mean height is the mean surface roughness

FUNCTIONAL ASPECTS OF SURFACE ROUGHNESS

The surface roughness of a material can have a significant functional impact on the material, depending on the surface features, the type of material, and its application. The following will identify some examples of the functional impacts of surface roughness on material properties and functionality.

Wettability. The surface wettability of a material plays a key role in various fields. Thus, controlling the wettability of a surface is desired for a range of applications. Surface can be prepared, which are not easily wet by aqueous media (hydrophobic surfaces), non-polar media (oleophobic surfaces), or both (amphiphobic surfaces). These types of surfaces are often prepared by introducing surface roughness. In one example, films were made with a blend of surface-functionalized poly(methyl methacrylate) and polyvinylidene difluoride (PVDF). [9] The surface showed a rough relief, using an Olympus LEXT confocal microscope using 405 nm laser light, which often occurs in films of polymer blends (**Figure 3**A). The surface is hydrophobic, demonstrated by the high contact angle of water on the surface. Upon application of an electric field, the piezoelectric response of PVDF causes the film to become smoother (**Figure 3**B), and the surface is better wet by water, and the wetting contact angle decreased. Thus, the coating displayed a reversibly hydrophobic surface using an electric field as the stimulus.

Additionally, super-hydrophobic and oleophobic surfaces on aluminum alloy substrates were achieved by chemical etching, followed by the deposition of an organosilicate. The surface roughness achieved through chemical etching was optimized to a surface roughness to achieve hydrophobicity, and oleophobicity was achieved due to air entrapment at the oil-surface interface. This topic is presented in detail in the digest article "Super-hydrophobic and Oleophobic Aluminum Alloy Surfaces via Chemical Etching and Functionalization."

Friction Resistance. The surface of a material also has import implications on its ability to resist friction. In terms of dry friction, the beneficial effects of surface structures can be mainly attributed to the storage of wear debris and a reduced contact area. [10] Amanov et al. showed a reduction in Cu alloy surfaces' friction coefficient with patterned bulges due to the reduced contact surface area. [11] With lubrication, the reduced friction associated with rough and textured surfaces can be attributed to the accumulation of wear particles to create conformal interfaces, [12] lubricant reservoirs in the textured surface features, and additional hydrodynamic pressure. [10, 13] In the article digest "Effects of Multi-Scale Patterning on the Run-In Behavior of Steel–Alumina Pairings under Lubricated Conditions" Grützmacher et al. showed the effect of large-scale micro-coined features and small-scale laser patterning features of steel–alumina pairings under lubricated conditions. [10]

Optical Properties. Surface roughness features can be used to tune the optical properties of a surface, such as reducing reflection, or increasing scattering. Surface roughness can be used to achieve better light trap-

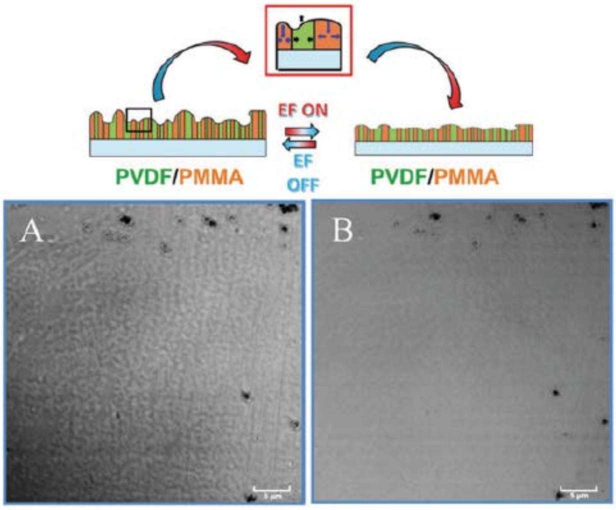

Figure 3: Confocal images, using an Olympus LEXT microscope using 405 nm laser, of the PVDF/PMMA surface A) without and B) with the application of external voltage (EF intensity = 1 V µm−1). The top part of the image gives the schematic representation of the proposed mechanism of surface smoothening. Reproduced with permission from Ref. [9].

ping and absorptance in solar cells to improve solar energy conversion efficiency. Light trapping can compensate for short optical path lengths and minority carrier diffusion lengths in thin light absorbers. Light trapping increases the amount of absorbed light in thin absorbers. Randomly textured transparent conductive oxides (TCO) are commonly used in silicon thin-film solar cells as front contacts. The TCOs' surface textures assist in reducing reflection losses and increasing scattering/diffraction of the incident light. [14]

Additional optical properties are dependent on material surface roughness and texture, including the gloss reflectance of materials. For example, Vessot et al. showed a strong correlation between surface texture and the gloss reflectance of photographic paper using confocal microscopy. Examples of surface textures of photographic paper obtained using an Olympus LEXT OLS4000 confocal microscope with different objective lenses are shown in **Figure 4**. [15]

Anti-scaling Properties. The surface roughness of a material also has an impact on its potential to resist fouling or scaling. In addition to surface roughness, the chemical composition, adsorption characteristics, charge, and nanostructure of the surface can modify the surface energy and, thus, the adhesion between the material and the scaling particles. In scaling, surface nucleation sites on the surface must be present. The presence of free and active nucleation sites depends mostly on the topography and roughness of the material. Thus, it has been demonstrated that the best anti-scaling surfaces have the lowest surface roughness. [16]

Corrosion Resistance. The corrosion resistance of metals, such as stainless steel, is correlated with its surface topography, which has important implications for product lifetime. [17] For example, Pistorius and Burstein showed that more corrosion pits formed on the rougher surface and concluded that deep depressions on steel surfaces have a lower potential to activate corrosion than surfaces which contain more open pits because of different diffusion rates. [18] Interestingly, Li et al. reported that Cu surface roughness resulted in local fluctuations in the electron-work function, which act as surface microelectrodes, resulting in accelerated corrosion. [19] Conversely, Hagen et al. found that surface roughness and asperities can be beneficial to corrosion resistance when utilizing a polymer coating. They found that increasing roughness on surfaces with triangular peaks increased the effective contact area and decreased the corrosive delamination. [20]

Sensor Activity. The surface properties of materials also have an impact on their performance in sensor applications. As an example, Yin et al. fabricated ZnO hollow nanospheres under different conditions that vary the surface roughness. The particles were utilized in chemiresistance sensors for alcohol vapors. The authors found that the roughest sample gave the best sensor response toward alcohol vapor. The improved response with the introduction of surface roughness was attributed to factors including the introduction of beneficial atoms in the surface features, improved crystalline quality, and the presence of many surface adsorption sites. [21]

Electronic Devices. Surface roughness plays an important role in the properties and function of electronic devices. This is particularly true for thin film electronics, where the size of the surface roughness features approaches the finite film thickness and edge/surface effects contribute more to the bulk material properties. Electron scattering at the boundaries becomes important in thin metallic films and increases with increasing surface roughness resulting in increased resistance. [22] For example, Luo et al. showed that the resistivity of silver films, deposited under different conditions to vary the surface roughness, increased with increasing roughness. [23]

Moreover, the existence of surface roughness on capacitor electrodes can increase the leakage current. This is due to the exponential relationship between leakage current and electric field. Rough features on electrodes result in an inhomogeneous electric field, and high leakage current at points where the local electric field is high. [22]

CONCLUSIONS

To conclude, surface roughness is an important material property that significantly impacts material properties and functionality in myriad applications. Although traditional methods of measuring surface roughness have been able to characterize a variety of surface features, LSCM provides the most encompassing solution to surface metrology. LSCM requires minimal sample preparation and can image virtually any material. Also, LSCM is inherently faster than SEM or AFM; it delivers very high-resolution and high-contrast images and has a high angle of detection capabilities to image steep interfaces. Moreover, LSCM uniquely enables the measurement of areal surface parameters. Surface parameters provide more information than profile-based methods and are more representative of the sample. Finally, examples have been provided that show the functional impacts of surface roughness for various applications, including wettability, friction resistance, optical properties, anti-scaling performance, corrosion resistance, sensor activity, and electronic properties.

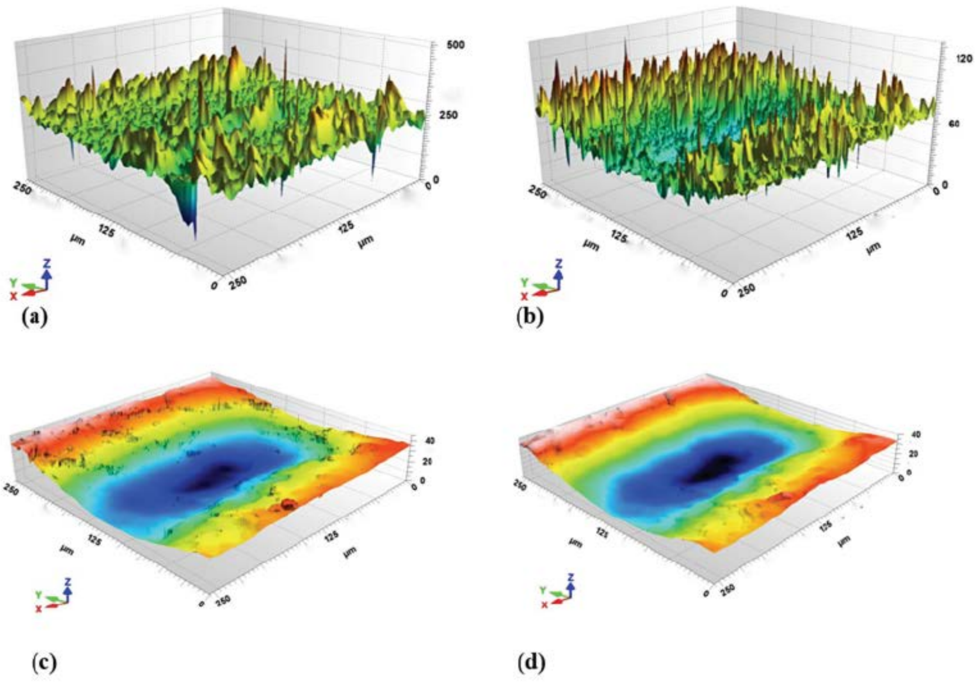

Figure 4: Surface textures cropped to an identical region of photographic paper collected with an using an Olympus LEXT microscope using different objective lenses: (a) 5×, (b) 10×, (c) 20×, and (d) 50×. Reproduced with permission from Ref. [15].

REFERENCES

[1] *X. Teng, F. Li, C. Lu, Visualization of materials using the confocal laser scanning microscopy technique, Chem. Soc. Rev., **2020**, 49 2408-2425.*

[2] *D.A. Lange, H.M. Jennings, S.P. Shah, Analysis of surface roughness using confocal microscopy, J. Mater. Sci., **1993**, 28 3879-3884.*

[3] *M. Fabich, Advancing Confocal Laser Scanning Microscopy, Opt. Photonik, **2009**, 4 40-43.*

[4] *Introduction to Surface Roughness Measurement, Olympus Corporation, Tokyo, Japan, **2020**, pp. 1-48.*

[5] *I. Calandra, L. Schunk, A. Rodriguez, W. Gneisinger, A. Pedergnana, E. Paixao, T. Pereira, R. Iovita, J. Marreiros, Back to the edge: relative coordinate system for use-wear analysis, Archaeol. Anthropol. Sci., **2019**, 11 5937-5948.*

[6] *F. Blateyron, The Areal Field Parameters, **2013**, 15-43.*

[7] *F. Marinello, A. Pezzuolo, Application of ISO 25178 standard for multiscale 3D parametric assessment of surface topographies, IOP Conf. Ser.: Earth Environ. Sci., **2019**, 275 012011.*

[8] *S. Stach, W. Sapota, Z. Wróbel, Ş. Ţălu, Assessment of possibilities of ceramic biomaterial fracture surface reconstruction using laser confocal microscopy and long working distance objective lenses, Microsc. Res. Tech., **2016**, 79 385-392.*

[9] *O. Guselnikova, J. Svanda, P. Postnikov, Y. Kalachyova, V. Svorcik, O. Lyutakov, Fast and Reproducible Wettability Switching on Functionalized PVDF/PMMA Surface Controlled by External Electric Field, Adv. Mater. Int., **2017**, 4 1600886.*

[10] *P.G. Grützmacher, A. Rosenkranz, A. Szurdak, C. Gachot, G. Hirt, F. Mücklich, Effects of Multi-Scale Patterning on the Run-In Behavior of Steel–Alumina Pairings under Lubricated Conditions, Adv. Eng. Mater., **2018**, 20 1700521.*

[11] *A. Amanov, R. Tsuboi, H. Oe, S. Sasaki, The influence of bulges produced by laser surface texturing on the sliding friction and wear behavior, Tribol. Int., **2013**, 60 216-223.*

[12] *A. Kovalchenko, O. Ajayi, A. Erdemir, G. Fenske, Friction and wear behavior of laser textured surface under lubricated initial point contact, Wear, **2011**, 271 1719-1725.*

[13] *A. Borghi, E. Gualtieri, D. Marchetto, L. Moretti, S. Valeri, Tribological effects of surface texturing on nitriding steel for high-performance engine applications, Wear, **2008**, 265 1046-1051.*

[14] *Ľ. Scholtz, L. Ladanyi, J. Müllerová, Influence of surface roughness on optical characteristics of multilayer solar cells, **2014**.*

[15] *K. Vessot, P. Messier, J.M. Hyde, C.A. Brown, Correlation between gloss reflectance and surface texture in photographic paper, Scanning, **2015**, 37 204-217.*

[16] *H. Kiepfer, W. Omar, T. Schröder, H.-J. Bart, Polymer Film Heat Transfer Surfaces in Seawater Desalination: Fouling Layer Formation and Technology, Chem. Eng. Technol., **2020**, 43 1205-1213.*

[17] *S.M. Lee, W.G. Lee, Y.H. Kim, H. Jang, Surface roughness and the corrosion resistance of 21Cr ferritic stainless steel, Corros. Sci., **2012**, 63 404-409.*

[18] *P. Pistorius, G. Burstein, Metastable pitting corrosion of stainless steel and the transition to stability, Philos. Trans. R. Soc. Lond., A: Phys. Eng. Sci., **1992**, 341 531-559.*

[19] *W. Li, D. Li, Influence of surface morphology on corrosion and electronic behavior, Acta Mater., **2006**, 54 445-452.*

[20] *C.M.H. Hagen, A. Hognestad, O.Ø. Knudsen, K. Sørby, The effect of surface roughness on corrosion resistance of machined and epoxy coated steel, Prog. Org. Coat., **2019**, 130 17-23.*

[21] *M. Yin, S. Liu, Preparation of ZnO hollow spheres with different surface roughness and their enhanced gas sensing property, Sens. Actuators B: Chem., **2014**, 197 58-65.*

[22] *Effects of Surface Roughness: Examples, in: Y. Zhao, G.-C. Wang, T.-M. Lu (Eds.) Experimental Methods in the Physical Sciences, Academic Press **2001**, pp. 309-351.*

[23] *E. Luo, S. Heun, M. Kennedy, J. Wollschläger, M. Henzler, Surface roughness and conductivity of thin Ag films, Phys. Rev. B, **1994**, 49 4858.*

01

Effects of Multi-Scale Patterning on the Run-In Behavior of Steel – Alumina Pairings under Lubricated Conditions

Philipp G. Grützmacher, Andreas Rosenkranz, Adam Szurdak, Carsten Gachot, Gerhard Hirt, and Frank Mücklich

ABSTRACT

The effect of multi-scale surfaces on frictional and wear performance was performed on a ball-on-disk tribometer under lubricated conditions using additive-free poly-alpha-olefine oil. Multi-scale stainless steel samples (AISI 304) were prepared by micro-coining and subsequent, direct laser interference patterning. A comparison of different samples (i.e., polished reference, laser-patterned, micro-coined, and multi-scale) shows a clear influence of the fabrication technique on the tribological properties. For multi-scale structures, the structural depth from the micro-coining plays an important role. Multi-scale samples with lower coining depths (50 µm) showed an increased coefficient of friction compared to the purely micro-coined surfaces, whereas larger coining depths (95 µm) result in stable and lower friction values for the multi-scale patterns.

INTRODUCTION

Friction is a multi-scale phenomenon affected by various factors such as adhesion, deformation, fracture, and third-body interactions ranging from nanometer to millimeter scale. [1] This scale dependency is well known and manifests when measuring the coefficient of friction (COF) at the nano- and macro-scales. [2,3] The question that arises is how to overcome this multi-scale phenomenon and manipulate friction on different scales. Nature accomplishes this by creating hierarchical surface patterns. [1,4–6] In bio-mimetics, this design idea is used to create well-defined surfaces with specially tailored frictional properties. [7]

The tribological effectiveness, under dry and lubricated conditions, of single scale surface features has been demonstrated. [8–11] In terms of dry friction, the beneficial effects of surface structures can be mainly traced back to the storage of wear debris and a reduced contact area. [12,13] Under lubricated conditions, the improvements can be attributed to the storage of produced wear particles, [14] a reservoir effect for lubricants, [15] and hydrodynamic pressure build-up. [16]

There are various methods to manufacture artificial topographies with variable pattern parameters such as structural depth, pitch, diameter, or area density, including lithographic techniques, [17] embossing/coining, [18] and laser surface texturing. [19] Laser surface texturing and, in particular, direct laser interference patterning (DLIP) is a suitable technique to structure various materials with patterns having mm and even sub-mm features. [20] To produce larger feature sizes on metallic substrates, coining/embossing seems to be a viable process route, which also offers mass production capability. [21]

Despite the fact that nature demonstrates plenty of beneficial effects for multi-scale surface patterns, those patterns have been rarely investigated in terms of their frictional and wear behavior. Most of the tested patterns are “multi-shape” structures combining at least two pattern geometries with similar dimensions. Therefore, the goal of this research work is to investigate the frictional and wear performance of multi-scale surfaces combining a larger micro-coined surface pattern with a cross-like laser surface pattern (DLIP). The tribological behavior of the produced multi-scale surface patterns is compared to single-scale micro-coined and laser patterns.

METHODS

Stainless steel (AISI 304) blanks with a thickness of 1 mm (0.04 in.) and a polished surface (root mean square roughness Rq = 30 nm) were used. The samples were ultrasonically cleaned for 10 min. in cyclohexane, acetone, and then isopropanol.

Micro-coining is a forming process in which a pre-structured tool is used to imprint the tool's pattern into the surface of a workpiece. To coin high strength materials, the workpiece needs to be heated up to reduce the flow stress, decreasing the die load. The current density and heating time were set to 35 A mm^{-2} and 5 s, respectively. This leads to a maximum sample temperature of ~1200 °C (2192 °F). First, the sample is heated by conductive heating. Afterward, the sample gets cut and coined in one tool movement at 5 mm s^{-1}. Circular dimples with structural depths of 50 µm and 95 µm, diameters of 181 µm and 212 µm, as well as a pitch of 558 µm, were fabricated (called A2 and A3, respectively). Polished reference samples were coined with a flat die keeping all coining parameters constant.

A high-power, solid-state, neodymium-doped (Nd) glass YAG laser with a pulse duration of 10 ns, a wavelength of 355 nm, and a repetition rate of 10 Hz was used for DLIP. The laser fluence was a constant 29 J cm^{-2} for all samples. By using two interfering sub-beams, line-like surface topography is induced. Well-defined, cross-like surface topography with a periodicity of 9 µm and a structural depth of 1 µm was obtained. To create the cross-like pattern, the samples are structured with two line-like patterns which are rotated by 90° relative to each other. Multiscale samples were first coined and subsequently superimposed by a cross-like laser pattern.

The samples' topography was characterized by laser scanning microscopy (Olympus® LEXT™ OLS4100 laser scanning confocal microscope) to study the surface roughness and the quality of the patterns. The tribological tests were done using a ball-on-disc tribometer in rotational sliding mode with a constant normal force of 5 N and a track radius of 5 mm (0.2 in.). The tribological counter body was an aluminum oxide (Al_2O_3) ball with a diameter of 6 mm (0.24 in.). The estimated Hertzian contact pressure is ~1.29 GPa. The sample is located in a rotating lubricant containment filled with 7 mL of polyalphaolefine (PAO 40) oil. Linear variable differential transducers measured the friction force. A sliding velocity of 0.01 m s^{-1} was selected for this study.

RESULTS AND DISCUSSION

The coined surfaces are analyzed before and after DLIP using LSM. As shown in **Figure 1**c and **Figure 1**d, the small structures with a depth of ~1 µm created by DLIP are homogeneously distributed over the entire sample with features on the fillets between the dimples, as well as inside the dimples. The two different coined patterns are produced with the same die but varying coining pressures.

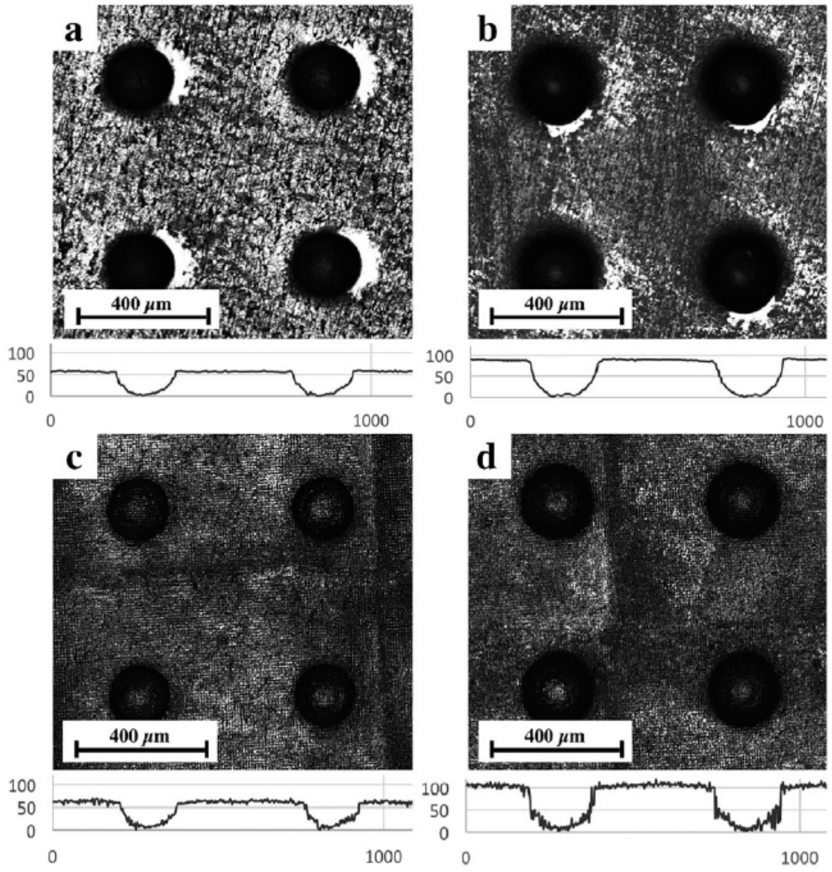

Figure 1: Overview as well as profile information of the coined samples a), c) A2 and c), d) A3, respectively. The top view as well as the profiles are shown before a), b) and after laser patterning c), d). All data are given in µm.

Figure 2 summarizes the COF's temporal evolution for the polished reference, the purely coined (A2), and laser-patterned samples. The figure shows the frictional behavior of the corresponding multi-scale sample (A2). The polished reference sample starts with a COF of ~0.11 and stays constant over the entire measuring time of 200 sliding cycles. The smooth trend of the COF, without any increase, combined with the fact that no pronounced wear tracks can be observed for the reference (**Figure 3**) at a sliding velocity of 0.01m s^{-1} leads to the conclusion that the prevailing lubrication regime can be assigned to elastohydrodynamic lubrication (EHL). This goes hand in hand with the estimated nominal Hertzian contact pressure of 1.29 GPa. This implies that elastic deformation of the rubbing surfaces and a viscosity increase with pressure become relevant. [22]

As can be seen in **Figure 2**, the COF of the laser-patterned sample starts at ~0.20 and decreases in the first 75 sliding cycles. Afterward, the sample reaches steady-state conditions. The observed effects can be attributed to the wearing-off of the highest surface asperities during the laser pattern's run-in and degradation. [10] The increased surface roughness and spiky surface topography increase the contact pressure, which makes a transition from full-film EHL to mixed lubrication. [8] Furthermore, the laser-patterned surface's load-bearing capacity is reduced compared to the plateau-like surface of the reference, which can also lead to more pronounced wear features and an increased wear rate. The laser pattern effects lead to the generation of wear particles and a modified contact area, which results in a higher COF over time. [23,24]

The COF of A2 starts at ~0.07 and shows a slight increase in the first sliding cycles. This can be explained by an initial high wear rate in which the sharpest asperities are worn off. [25] After a decrease of the COF in the subsequent cycles, the COF remains relatively constant at ~0.05. Compared to the polished reference, A2 leads to a friction reduction by a factor of ~2. The significant friction reduction can be explained by a pressure build-up and an additional oil supply from the surface structures. [22]

As shown in **Figure 2**, the respective multi-scale pattern (coining A2 and DLIP) shows worsened frictional behavior compared to the purely coined sample. The initial COF is ~0.10 and decreases to ~0.08. Compared to the polished reference, the multi-scale surface shows a ~20% decrease in COF. However, compared to the purely micro-coined surface, the COF of the multi-scale pattern is ~60% higher.

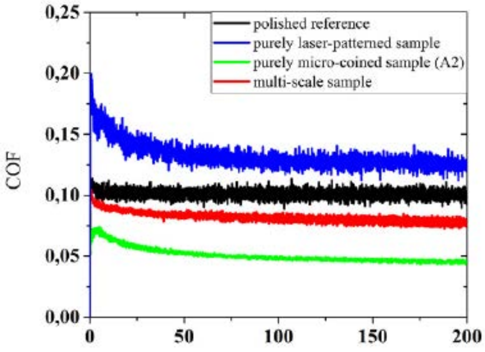

Figure 2: Temporal evolution of the COF of the polished reference, the purely coined sample (A2), the purely laser-patterned sample and the multi-scale sample.

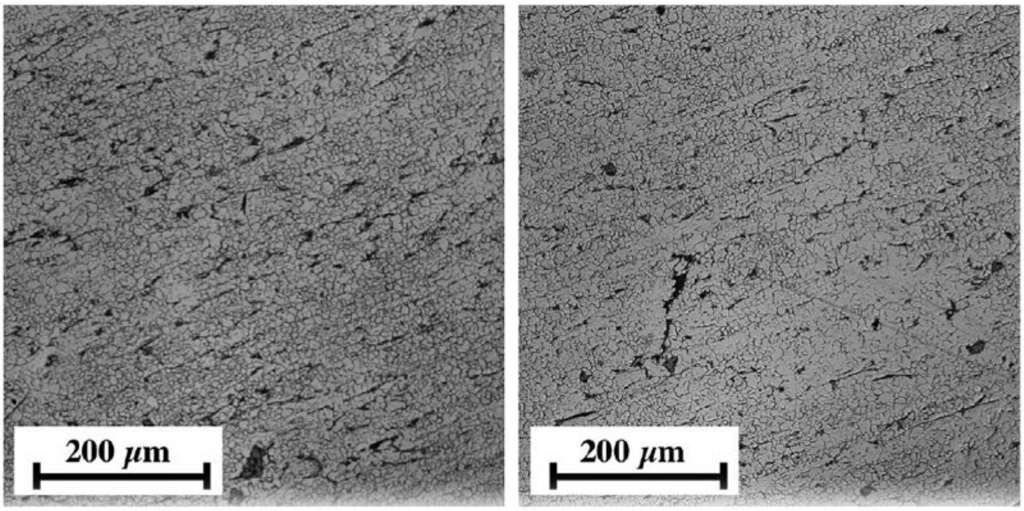

Figure 3: Surface of the polished reference after 200 sliding cycles at two different positions imaged by LSM.

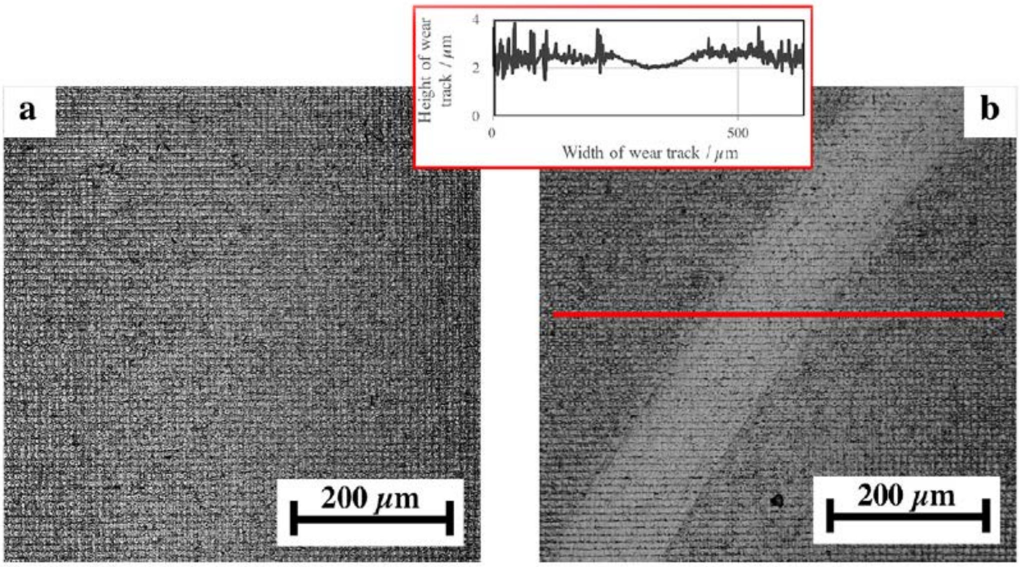

Figure 4: Images of the purely laser-patterned sample captured by LSM a) before and b) after the friction experiment with 200 cycles. The inset in the red box shows the wear track along the red line

To explain the worsened frictional behavior of the multi-scale surface, the wear behavior of those samples needs to be examined. **Figure 5** shows the entire wear track of the multi-scale surface (combining A2 and the laser pattern). The multi-scale surface shows a well-pronounced wear track. As a consequence, it can be assumed that the additional cross-pattern results in an increased contact pressure due to the rougher topography compared to the micro-coined samples. This can lead to undesired edge effects and stress raisers. Further, the alumina ball's deflection from its track is prominent, where it encounters several coined dimples in a row (see blue colored rectangle). The deflection of the ball might occur due to pressure build-up in the structures due to a converging gap that is formed between the ball and the structure.

Figure 6 summarizes the temporal evolution of the COF of the reference, the purely coined (A3), the laser-patterned samples, and the multi-sale sample (A3 combined with laser-patterning). The initial COF of A3 is ~0.17 and then decreases to ~0.11. Com-

Figure 5: The entire wear track of multi-scale sample (DLIP and coining A2) recorded by LSM. Additionally, a magnified LSM micrograph of an individual multi-scale structure is shown.

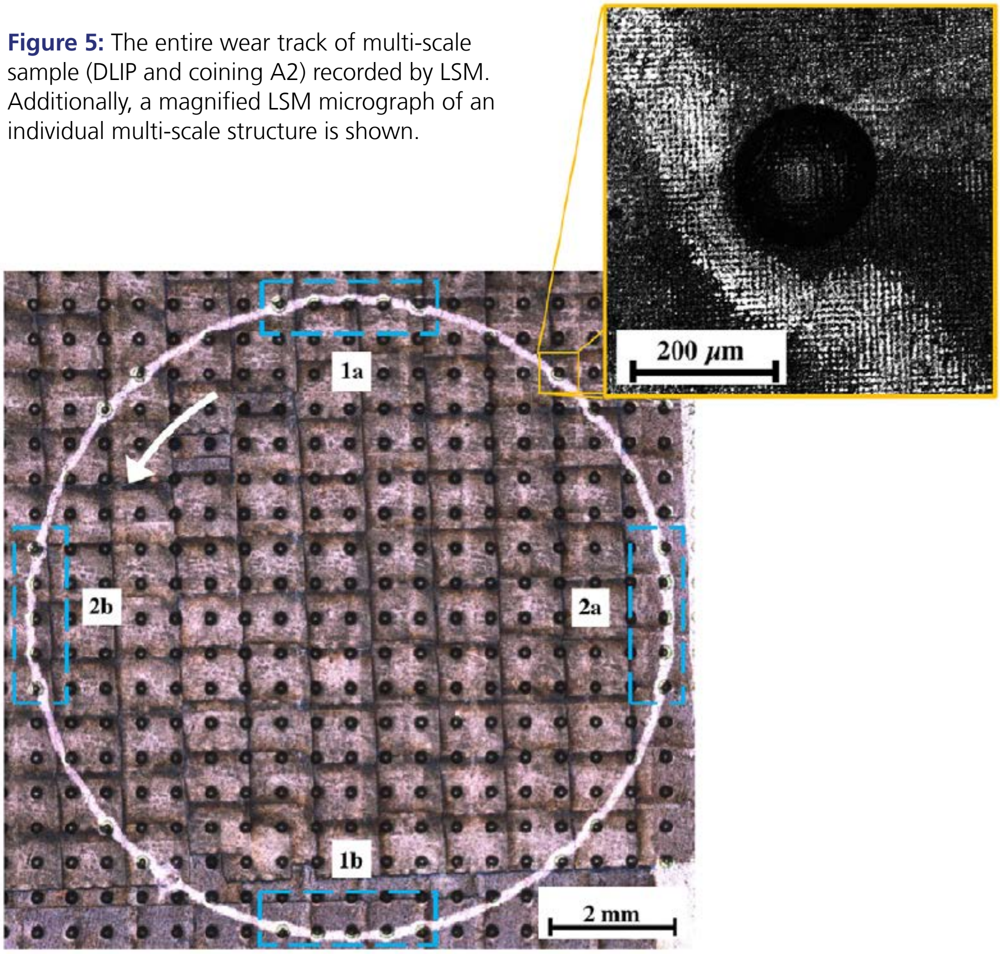

pared to A2, the COF of A3 is greater. For the polished reference, the COF of sample A3 is significantly increased in the first 50 sliding cycles. In the following sliding cycles, the COF of the reference and A3 are rather similar. Surface structures with a larger structural depth have a higher probability for cavitation, thus reducing the oil film thickness and load-bearing capacity. [22,26]

The initial COF of the multi-scale surface is ~0.11. After a slight decrease in the COF, the COF remains constant at ~0.10. It can be assumed that the cross-pattern helps to reduce pronounced cavitation due to a better lubricant distribution in the contact zone. By reducing cavitation, a larger local oil film thickness can be present, improving the load-bearing capacity and reducing the COF.

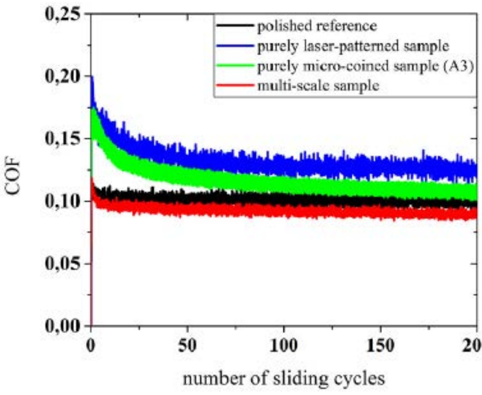

Figure 6: Temporal evolution of the COF of the polished reference, the purely coined sample (A3), the purely laser-patterned sample, and the multi-scale sample.

Figure 7: The entire wear track of multi-scale sample (DLIP and coining A3) recorded by LSM. Additionally, a magnified LSM-micrograph of an individual multi-scale structure is given.

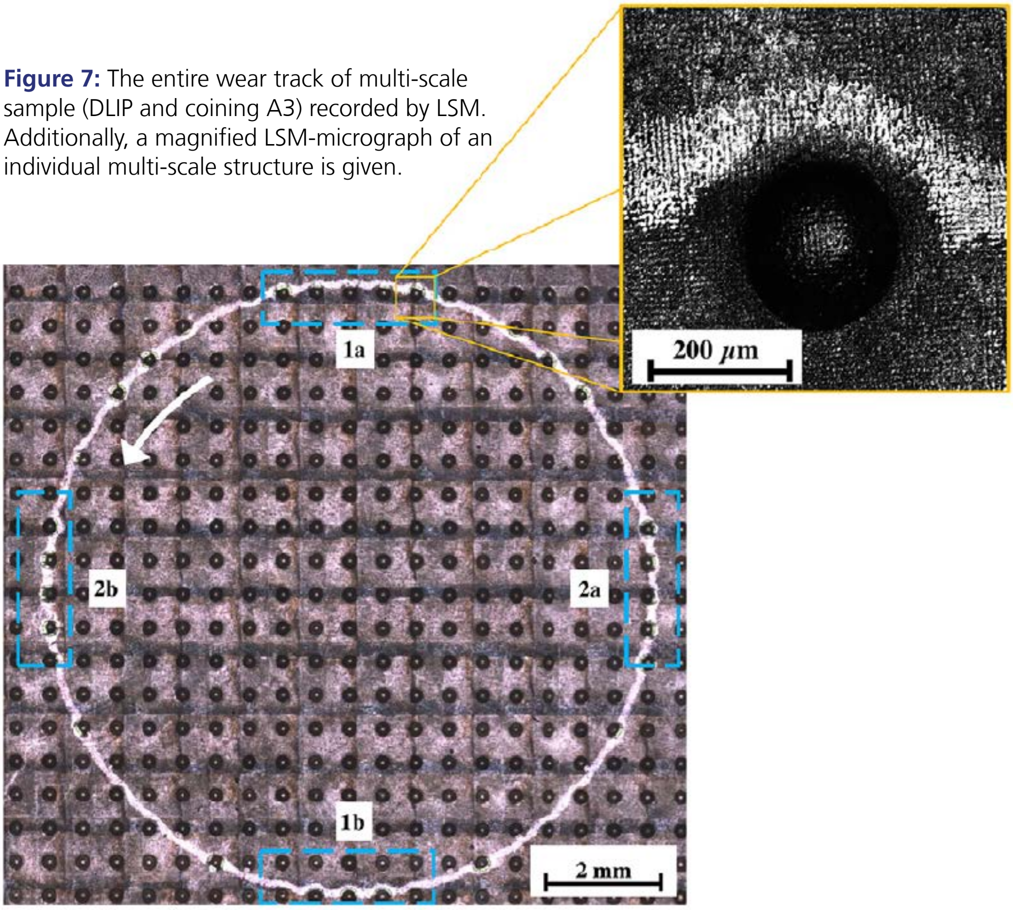

Figure 7 shows the wear behavior of the multi-scale pattern (A3 and laser-pattern) imaged by LSM. The deflection of the alumina ball from its track is prominent at the positions where it encounters several coined dimples in a row. Compared to the purely laser-patterned samples, the multi-scale patterns show a considerably reduced wear with a still intact laser-pattern after 200 sliding cycles. Wear behavior differences can be attributed to different lubrication regimes for the laser-patterned samples (mixed lubrication) and the multi-scale surfaces (mixed EHL).

CONCLUSIONS

To conclude, we found that the coined structures' depth determines whether the multi-scale patterns have a beneficial or detrimental frictional effect. The COF of the multi-scale pattern is decreased for deep structures (95 µm) and increased for shallower ones (50 µm). Further, laser-patterned samples show an increased COF due to the spiky surface topography, which increases the contact pressure and causes the transition from full-film EHL to mixed lubrication. For the purely micro-coined surfaces, lower coining depths lead to the best tribological performance due to a pressure build-up in the lubricant and additional oil supply in the coined pockets. In contrast, the corresponding multi-scale sample shows worsened behavior due to increased surface roughness. The larger coined surfaces are less efficient over the entire measuring time because the deeper dimples are more prone to pronounced cavitation and do not allow for a sufficient pressure build-up. The multi-scale surfaces show advantageous effects and are characterized by a stable and relatively low COF. The additional laser patterns help reduce cavitation and therefore contribute to enhanced lubrication in the contact zone.

REFERENCES

[1] *M. Nosonovsky, B. Bhushan, Mater. Sci. Eng. R Rep. 2007, 58, 162.*

[2] *E. Broitman, Friction 2014, 2, 40.*

[3] *J. R. Barber, Tribol. Lett. 2013, 49, 539.*

[4] *Z. Guo, W. Liu, B. L. Su, J. Colloid Interface Sci. 2011, 353, 335.*

[5] *B. Bhushan, Y. C. Jung, Prog. Mater. Sci. 2011, 56, 1.*

[6] *B. Bhushan, Philos. Trans. R. Soc. A Math. Phys. Eng. Sci. 2009, 367, 1445.*

[7] *H. Kasem, A. Tsipenyuk, M. Varenberg, Soft Matter 2015, 11, 2909.*

[8] *A. Rosenkranz, T. Heib, C. Gachot, F. Mücklich, Wear 2015, 334–335, 1.*

[9] *I. Etsion, Tribol. Lett. 2004, 17, 733.*

[10] *C. Gachot, A. Rosenkranz, L. Reinert, E. Ramos-Moore, N. Souza, M. H. Müser, F. Mücklich, Tribol. Lett. 2013, 49, 193.*

[11] *W. Tang, Y. Zhou, H. Zhu, H. Yang, Appl. Surf. Sci. 2013, 273, 199.*

[12] *A. Amanov, R. Tsuboi, H. Oe, S. Sasaki, Tribol. Int. 2013, 60, 216.*

[13] *B. Zhang, W. Huang, J. Wang, X. Wang, Tribol. Int. 2013, 65, 138.*

[14] *A. Kovalchenko,O. Ajayi, A. Erdemir, G. Fenske, Wear 2011, 271, 1719.*

[15] *A. Borghi, E. Gualtieri, D. Marchetto, L. Moretti, S. Valeri, Wear 2008, 265, 1046.*

[16] *D. Gropper, L. Wang, T. J. Harvey, Tribol. Int. 2016, 94, 509.*

[17] *U. Pettersson, S. Jacobson, Tribol. Lett. 2004, 17, 553.*

[18] *H. Ike, M. Plancak, J. Mater. Process. Technol. 1998, 80–81, 101.*

[19] *I. Etsion, J. Tribol. 2005, 127, 248.*

[20] *F. Mücklich, A. F. Lasagni, C. Daniel, Int. J. Mater. Res. 2006, 97, 1337.*

[21] *A. Szurdak, A. Rosenkranz, C. Gachot, G. Hirt, F. Mücklich, Key Eng. Mater. 2014, 611–612, 417.*

[22] *A. Rosenkranz, A. Szurdak, C. Gachot, G. Hirt, F. Mücklich, Tribol. Int. 2016, 95, 290.*

[23] *P. G. Grützmacher, A. Rosenkranz, S. Rammacher, C. Gachot, F. Mücklich, Tribol. Int. 2017, 116, 256.*

[24] *A. Rosenkranz, L. Reinert, C. Gachot, F. Mücklich, Wear 2014, 318, 49.*

[25] *P. J. Blau, Tribol. Int. 2005, 38, 1007.*

[26] *M. B. Dobrica, M. Fillon, M. D. Pascovici, T. Cicone, Proc. Inst. Mech. Eng. Part J J. Eng. Tribol. 2010, 224, 737.*

Copyright:
DOI: 10.1002/
adem.201700521;
Philipp G. Grützmacher,
Andreas Rosenkranz,
Adam Szurdak, Carsten
Gachot, Gerhard Hirt,
Frank Mücklich; Advanced
Engineering Materials;

02

Super-Hydrophobic and Oleophobic Aluminum Alloy Surfaces via Chemical Etching and Functionalization

Andreia Rocha Canella Carneiro, Fábio Augusto de Souza Ferreira, and Manuel Houmard

ABSTRACT

Super-hydrophobic and oleophobic surfaces on ASTM 1200 H14 aluminum alloy substrates were achieved by chemical etching followed by the deposition of organically modified silicate coatings. The chemical etching solutions iron(III) chloride + hydrogen chlorine + hydrogen peroxide ($FeCl_3 + HCl + H_2O_2$) and etching time were varied to increase the surface roughness. The chemical etching produces rough surfaces with superficial square pores and edges about 1 µm–2 µm. The chemical modifications modified silicate solutions based on perfluorooctyltriethoxysilane (PFOTES) and hexadecyltrimethoxysilane (HDTMS) sol-gel precursors induced water contact angles about 154° and 150°, respectively. Moreover, the surface modification based on PFOTES demonstrated an oleophobic character with an oil contact angle of 136° due to air entrapment in the surface roughness at the oil-aluminum interface.

INTRODUCTION

In the last decades, the development of super-hydrophobic surfaces has received attention due to their interesting properties and potential applications on the surface of metals, ceramics, and polymers. [1–12] Such surfaces exhibit almost no interaction with water, showing contact angles higher than 150°. [13] Some benefits of super-hydrophobic surfaces include easy cleaning, anti-adherence, and corrosion resistance. [4,13] Thus, the production of surfaces with such properties on aluminum alloys has attracted particular interest due to the many potential applications of such a light metallic substrate, especially to increase corrosion protection. [14] Further, the control over the wettability of organic and apolar fluids such as oil, is also sought for many applications. [4,15,16] In this context, various studies have been carried out to create surfaces that are both super-hydrophobic and super-oleophobic. Such surfaces, called super-amphiphobics, can repel both water and oil. [17–19] These surfaces are commonly prepared by increasing surface roughness and reducing surface energy. [8,20–23]

Several techniques create rough superficial structures on metals, including chemical etching, anodic oxidation, lithography, and deposition of nanoparticles. [18,24,25] Chemical etching, accelerated and controlled corrosion, [26] is commonly used because it is an easy and cheap method. [18] Aqueous solutions of iron (III) chloride ($FeCl_3$) have been used in industry as a chemical etching agent [27] for metals such as steel, aluminum, and copper alloys. [26] As an example, Liu et al. [1] produced superhydrophobic surfaces in AISI 304 stainless steel by creating a micro-/nanostructure, using an etching solution composed of $FeCl_3$ + HCl + H_2O_2 (FHH), followed by a coating deposition using the dodecyltriethoxysilane precursor. We applied this method to create a rough surface on an aluminum substrate for the first time.

Organically modified silicates (ORMOSIL) are organic-inorganic hybrid materials synthesized by hydrolysis and condensation reactions of organically modified silanes precursors. [28] The most straightforward class is formed from precursors with chemical formula as $RSi(OCH_3)_3$, where R is an organic terminal group that does not create bridges in the three-dimensional gel network. [29] In the case of hexadecyltrimethoxysilane (HDTMS) and 1H,1H,2H,2H-perfluorooctyltriethoxysilane (PFOTES) precursors, the R groups are composed of C–H and C–F bonds, respectively; they are responsible for the hydrophobic and oleophobic character of the functionalized materials.

Herein the surface of ASTM 1200 H14 aluminum alloy was chemically and morphologically modified with an etching treatment in the FHH solution [1] followed by the deposition of hybrid organic-inorganic coatings based on modified silica materials obtained by sol-gel process. PFOTES and HDTMS were used as alkoxide precursors to obtain the super-hydrophobic surface. The surface morphology was characterized by confocal microscopy, and contact angle measurements with deionized water and mineral oil were carried out to characterize the modified aluminum alloy surfaces' functionality.

METHODS

The ASTM 1200 H14 aluminum alloy sheets with a size of 60 mm × 40 mm × 0.3 mm (2.36 in. × 1.57 in. × 0.01 in.) were cleaned with acetone and deionized water in an ultrasonic bath for 5 minutes each. After cleaning, the samples were immersed in an FHH solution consisting of a mixture of iron (III) chloride aqueous solution with concentrations ranging from 0.05 mol L^{-1} to 0.50 mol L^{-1},

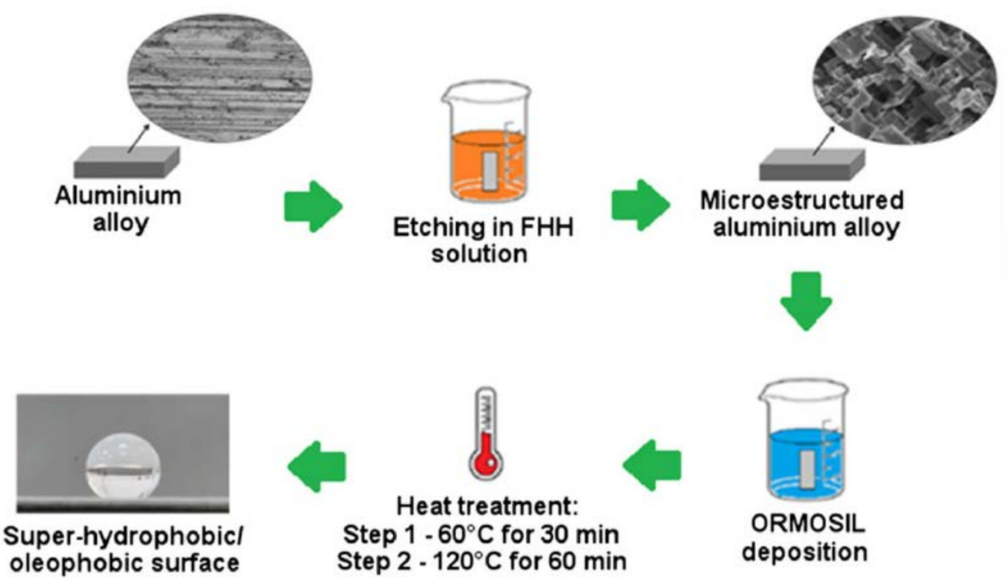

Figure 1: Schematic of the etching and ORMOSIL deposition.

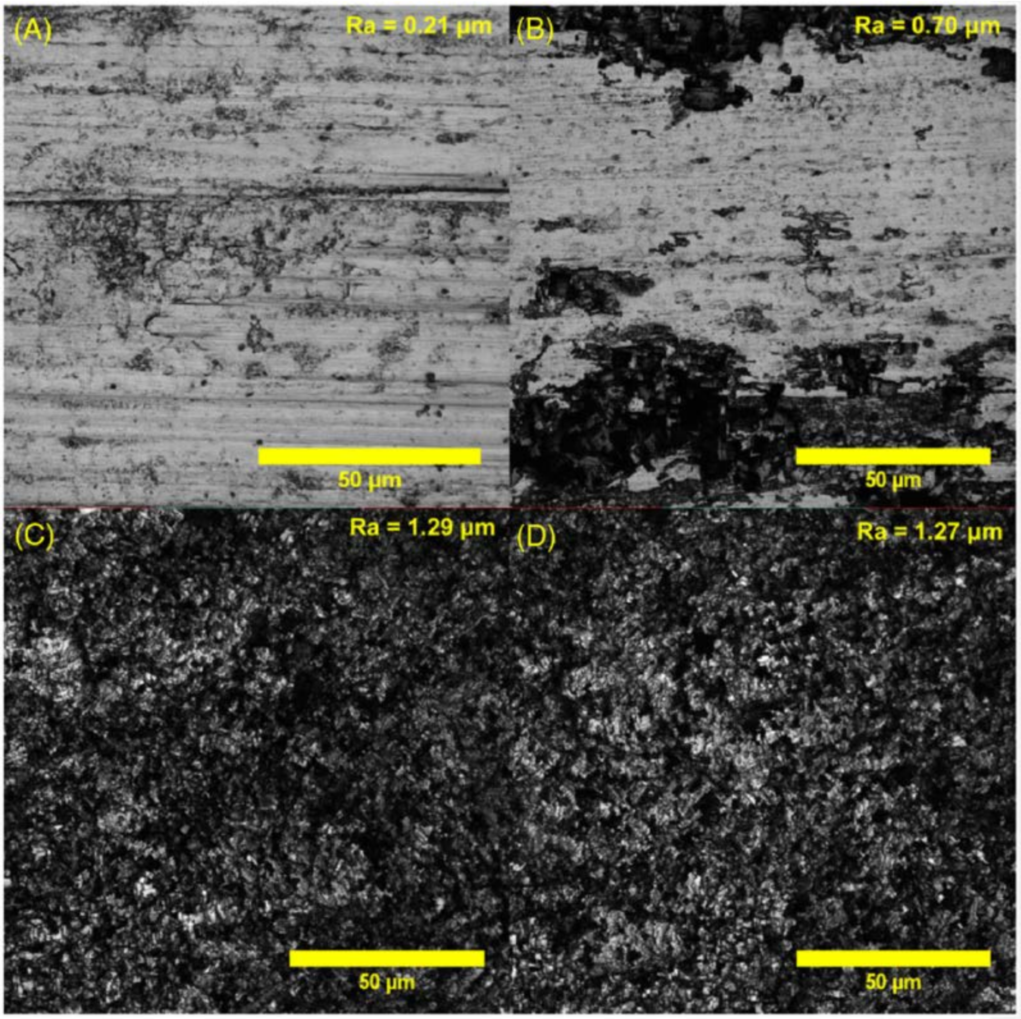

Figure 2: Confocal microscopy images and roughness values (Ra) of the (A) as-received aluminum surface, and chemically etched for 5 min in FHH solutions with $FeCl_3$ concentrations of (B) 0.05 mol L^{-1}, (B) 0.1 mol L^{-1}, and (D) 0.25 mol L^{-1}.

37% hydrochloric acid, and 35% hydrogen peroxide with volume proportion of 10:1:1, respectively. [1] The immersion times were 5, 7, 10, and 15 minutes. After etching, the samples were cleaned using a soft sponge, rinsed with deionized water, and washed with acetone and deionized water in an ultrasonic bath for 5 minutes. Then, water was removed with a hot air flow followed by drying in an oven for 20 minutes at 60 °C (140 °F).

ORMOSIL sol-gel solutions were prepared by hydrolysis and condensation of the hybrid precursors PFOTES and HDTMS in the presence of ethanol, deionized water, and 37% HCl. The molar ratio Precursor:EtOH:H2O:HCl was kept at 1:856:7.2:0.9. Coatings using TEOS and mixtures of TEOS with PFOTES as sol-gel precursors with the same molar proportions were also performed for comparison. Then, the sol-gel solutions were vigorously stirred for 2 minutes. The deposition was performed at room temperature using dip-coating. The deposited coatings were then heat-treated in an oven for 30 minutes at 60 °C (140 °F). Then, the oven temperature was raised to 120 °C (248 °F) for another 60 minutes. The chemical etching, followed by the deposition process of the ORMOSIL coating, is schematized in **Figure 1**.

The samples' surface morphology and roughness measurements were evaluated using a confocal microscope (Olympus® LEXT™ OLS4100 3D laser confo-

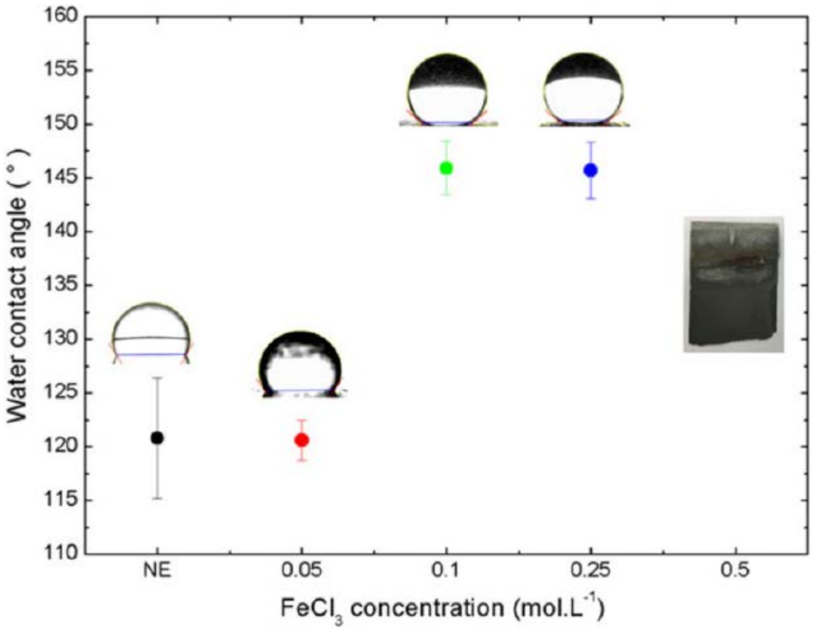

Figure 3: Water contact angle as a function of the FeCl3 concentration in the FHH solution for the samples etched for 5 min and for non-etched samples after PFOTES ORMOSIL deposition.

cal microscope). For the roughness measurements, a cut-off value of 80 µm and a Gaussian filter were selected. The chosen analysis parameter to quantify the roughness was the average roughness (Ra) determined from a cross-sectional line of 180 µm in length drawn along the surface samples.

The coating hydrophobicity and oleophobicity were quantified by water and oil contact angle (WCA and OCA) measurements using ~ 10 µL of deionized water and ~5 µL mineral oil, respectively. A portable optic tensiometer was used for the measurements.

RESULTS AND DISCUSSION

The $FeCl_3$ concentration of the FHH etching solution and the time of immersion was varied to optimize the aluminum substrates' roughness. Images obtained by confocal microscopy and the corresponding roughness values of the samples etched for 5 min in FHH solution with $FeCl_3$ concentrations of 0.05 mol L^{-1}, 0.1 mol L^{-1}, 0.25 mol L^{-1}, and 0.5 mol L–1 are presented in **Figure 2**. The as-received aluminum has a roughness Ra = 0.21 µm. The 0.05 mol L^{-1} $FeCl_3$ solution was not sufficient to create a uniformly rough surface, leading to a partial etching and Ra = 0.7 µm. For $FeCl_3$ concentrations of 0.1 mol L^{-1} and 0.25 mol L^{-1}, irregular and porous microstructures were uniformly formed over the entire surface, presenting higher Ra = 1.29 µm and Ra = 1.27 µm, respectively. The $FeCl_3$ concentration of 0.5 mol L^{-1} was also tested in this work; however, it caused excessive etching of the aluminum substrate.

Figure 3 shows the WCA as a function of $FeCl_3$ concentration in the FHH solution, followed by ORMOSIL coating from the PFOTES precursor. Non-etched (NE) and chemically etched samples with a $FeCl_3$ concentration of 0.05 mol L^{-1} showed similar average WCA values around 120°. The etched samples with a concentration of 0.1 mol L^{-1} and 0.25 mol L^{-1} showed relatively high WCAs, but not enough to reach for super-hydrophobicity (WCA > 150°). These results demonstrate that roughness really acts as a wettability amplifier, turning the hydrophobic character of the PFOTES ORMOSIL coating more hydrophobic.

The confocal microscopy images of the aluminum surfaces etched with a $FeCl_3$ concentration of 0.1 mol L^{-1} with immersion times of 5, 7, 10, and 15 minutes, and the corresponding Ra values are presented in

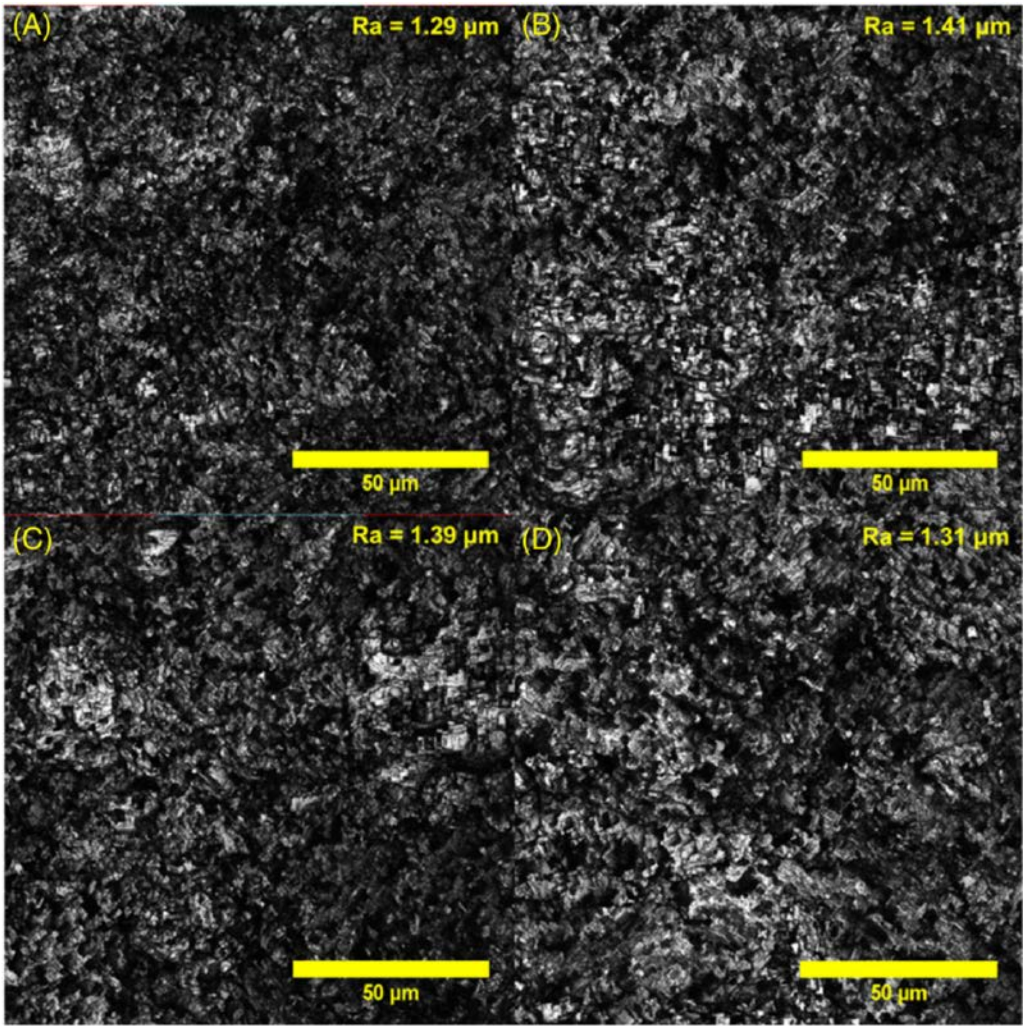

Figure 4: Confocal microscopy images and roughness values (Ra) of the chemically etched aluminum surfaces in the FHH solution with a FeC_{l3} concentration of 0.1 mol L^{-1} with etching times of (A) 5 min, (B) 7 min, (C) 10 min, and (D) 15 mi.

Figure 4. The images show that the morphologies are similar. However, the roughness slightly increases, followed by a gradual decrease as a function of the immersion time. For times greater than 7 minutes, the rough microstructure was slowly destroyed, decreasing the roughness until complete embrittlement.

In **Figure 5** are presented the WCA as a function of the etching time after PFOTES ORMOSIL deposition. It can be observed that all chemical etching with an immersion time of at least 5 minutes increased the hydrophobicity of the coated surface. However, only the time of 7 minutes provided the roughness necessary to obtain super-hydrophobicity, (WCA = 154.1°).

Figure 6 shows the WCA obtained for the uncoated samples and coated ones with the different ORMOSIL coatings and not-etched (NE) aluminum substrates. WCA measurements were also made on substrates coated with ORMOSIL based on TEOS precursor, which do not have hydrophobic groups, for comparison.

As-received and chemically etched substrates without ORMOSIL coating are hydrophilic (WCA < 90°). Non-etched aluminum substrates coated with ORMOSIL coating based on PFOTES and HDTMS became hydrophobic, with their contact angle increased to 120° and 110°, respectively. For etched and coated samples, the WCAs reached values above 150°. Such evidence demonstrates that the

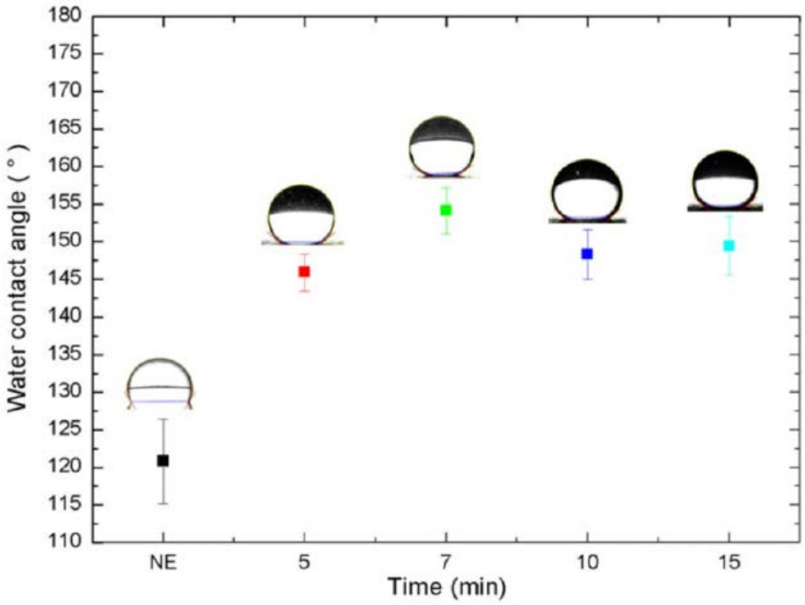

Figure 5: Water contact angle as a function of the chemical etching immersion time in the FHH solution with a $FeCl_3$ concentration of 0.1 mol L^{-1} and for non-etched samples after PFOTES ORMOSIL deposition.

rough surface enhanced the surface's intrinsic property, hydrophilic surfaces become more hydrophilic, and the hydrophobic surface becomes more hydrophobic, which is in agreement with the Wenzel model. [30] The high surface area of the rough surface (Wenzel model) or air trapped between the droplets and the rough hierarchical structure of the coated surface (Cassie-Baxter model) increased the hydrophobic property of the coating to reach a super-hydrophobic behavior. [30] Moreover, this behavior is also observed for the TEOS-coated samples, where the hydrophobicity increased for etched surfaces.

Figure 7 shows the mineral OCA measured with NE and etched aluminum substrates, uncoated (UC), and coated with ORMOSIL based on PFOTES and HDTMS. Compared with water wettability results, the values obtained are lower, suggesting a higher affinity of the surfaces with oil. This characteristic is justified considering the lower surface tension of mineral oil (30 mJ m^{-2}) than the water one (72 mJ m^{-2}). [57] The coated sample with PFOTES without etching exhibited oleophilic behavior (OCA <90°), which can be attributed to the van der Waals forces between the apolar alkyl chains and the mineral oil. The OCA of the same film deposited on an etched surface greatly increased to 137°. This result is in opposition to the Wenzel model that can only amplify the surface's intrinsic behavior, as mentioned previously. However, this behavior can be explained by the Cassie-Baxter model, where the air is entrapped in the material roughness, and the oil drop is deposited on a composite surface with oleophobic behavior. [30] The HDTMS-coated surfaces appeared to be oleophilic, both etched and NE substrates. The long apolar alkyl chains with only carbon and hydrogen atoms of HDTMS are responsible for the good spreading of oil. Moreover, the etching treatment of the aluminum surface-enhanced classically oleophilic property following the Wenzel model. In this case, we can infer that the surface is not oleophilic enough to let air pockets in the rough structure to repeal the oil spreading. On the contrary, due to a smaller dispersive component of its surface energy and high roughness, the PFOTES-coated sample succeeds to be super-hydrophobic and oleophobic. In this sense, the influence of the roughness shows again to be fundamental.

The TEOS ORMOSIL coating shows that the OCA values obtained on NE samples were about 30°. The smaller OCA measured for this sample, compared with the HDTMS and PFOTES coated ones, corroborate results discussed in previous work showing that the dispersive component of the surface energy, responsible

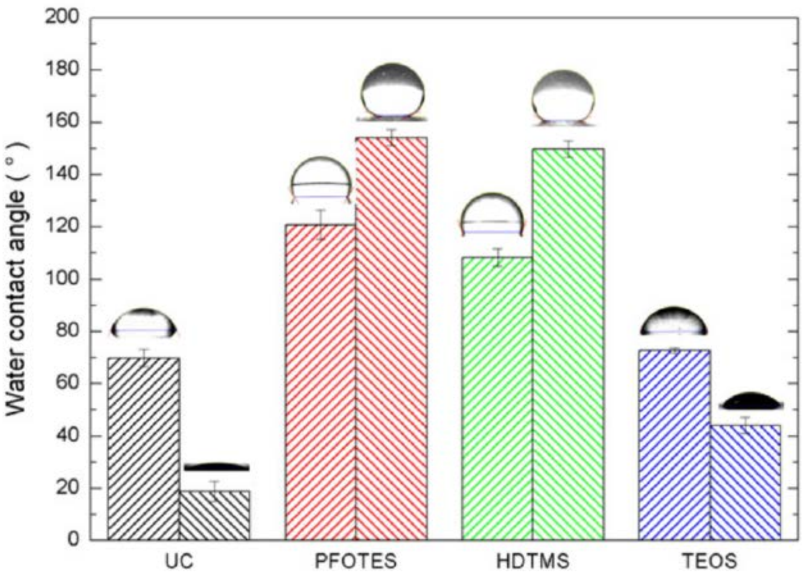

Figure 6: Water contact angles for uncoated (UC) and coated samples with ORMOSIL coatings on (///) non-etched and (\\\) etched aluminum substrates.

for the oil spreading, is higher for the surface with few alkyl chains than for the one with more of such groups. [31] Finally, as expected for such oleophilicity, the etching process increased the oil spreading on TEOS-coated surface, in agreement to the Wenzel model.

CONCLUSIONS

To conclude, super-hydrophobic and oleophobic coatings were fabricated on the surface of 1200 H14 aluminum alloy. The aluminum surface roughness was optimized via an etching treatment using an FHH solution. A $FeCl_3$ concentration of 0.1 mol L^{-1} and an immersion time of 7 min were determined to be optimal to enhance the surface roughness and the hydrophobicity after the deposition of ORMOSIL coatings using HDTMS and PFOTES sol-gel precursors. The etching treatment leads to a homogeneously rough surface with square pores with edges about 1 µm–2 µm. WCA measurements indicated that all etched surfaces functionalized with ORMOSIL showed super-hydrophobic properties. Finally, OCA showed that etched surfaces coated with s so-gel solution using PFOTES were oleophobic due to air entrapment at the oil-surface interface.

REFERENCES

[1] *Y. Liu, Y. Bai, J. Jin, L. Tian, Z. Han, L. Ren, Appl. Surf. Sci. 2015, 355, 1238.*

[2] *D.D., La, T.A. Nguyen, S. Lee, J.W. Kim, Y.S. Kim, Appl. Surf. Sci. 2011, 257 (13), 5705.*

[3] *L. Li, V. Breedveld, D.W. Hess, ACS Appl. Mater. Interfaces. 2012, 4 (9), 4549.*

[4] *T. Darmanin, F. Guittard, Mater. Today 2015, 15, 273.*

[5] *J.T. Simpson, S.R. Hunter, T. Aytug, Rep. Prog. Phys. 2015, 78 (8), 86501.*

[6] *A. Milionis, E. Loth, I.S. Adv. Colloid Interface Sci. 2016, 229, 57.*

[7] *Z. Wang, M. Elimelech, S. Lin, Environ. Sci. Technol. 2016, 50, 5, 2132.*

[8] *Q. Wen, Z. Guo Chem. Lett. 2016, 45 (10), 1134.*

[9] *E.V. Bryuzgin, V.V. Klimov, S.A. Repin, A.V. Navrotskiy, I.A. Novakov, Appl. Surf. Sci. 2017, 419, 454.*

[10] *C. Chen, S. Yang, L. Liu, et al., J. Alloys Compd. 2017, 711, 506.*

[11] *Z. Xu, Z. Liu, P. Song, C. Xiao Desalination. 2017, 414, 10.*

[12] *X. Zhao, B. Yu, J. Zhang, J. Colloid Interface Sci. 2017, 501, 222.*

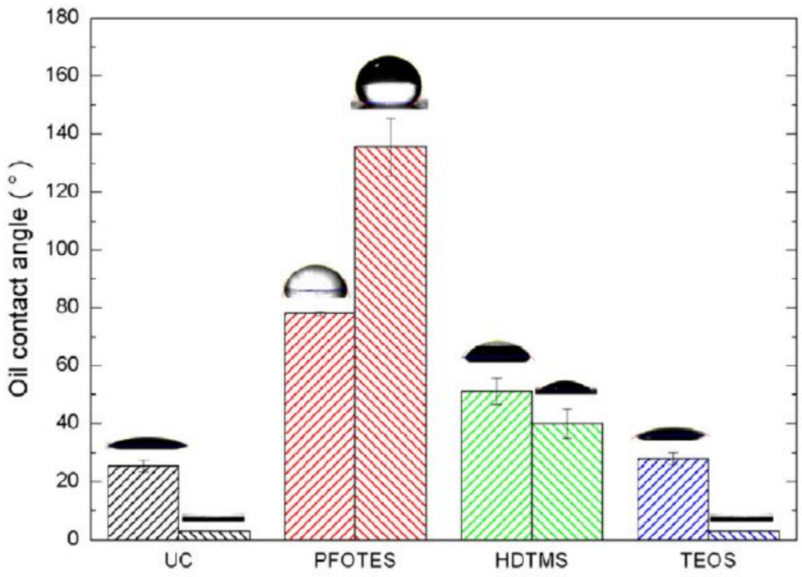

Figure 7:. Oil contact angles for uncoated (UC) and coated substrate with ORMOSIL coatings on (///) non-etched and (\\\) etched aluminum substrates.

[13] *H. Zhu, Z. Guo, W. Liu, Chem. Commun. 2014, 50 (30), 3900.*

[14] *R. Wu, G. Chao, H. Jiang, Y. Hu, A. Panm Mater. Lett. 2015, 42, 176.*

[15] *A. Vilcnik, I. Jerman, A.S. Vuk, et al., Langmuir 2009, 25 (10), 5869.*

[16] *Z.S. Saifaldeen, R. Khedir, K.R. Khedir, M.F. Cansizoglu, T. Demirkan, T. Karabacak, J. Mater. Sci. 2014, 49 (4), 1839.*

[17] *M. Nosonovsky, B. Bhushan, Curr. Opin. Colloid Interface Sci. 2009, 14 (4), 270.*

[18] *Z. Chu, S. Seeger, Chem. Soc. Rev. 2014, 43 (8), 2784.*

[19] *T. Jiang, Z. Guo, Chem. Lett. 2015, 44 (3), 324.*

[20] *M. Guo, B. Ding, X. Li, X. Wang, J. Yu, M.J. Wang, Phys. Chem. C 2010, 114 (2), 916.*

[21] *M. Ma, R.M. Hill, Curr. Opin. Colloid Interface Sci. 2006, 11 (4), 193.*

[22] *P. Zhang, F.Y. Lv, Energy 2015, 82, 1068.*

[23] *D. Lai, D. Kong, C. Che, Surf. Coat. Technol. 2017, 315, 509.*

[24] *R.G. Wankhede, M. Shantaram, K. Thanawala, A. Khanna, N. Birbillis, J. Mater. Sci. Eng. A 2013, 3, 224.*

[25] *D. Zhang, L. Wang, H. Qian, X. Li, J. Coat. Technol. Res. 2016, 13 (1), 11.*

[26] *O. Çakir, J. Mater. Process Technol. 2008, 199, 337.*

[27] *P.N. Rao, D. Kunzru, J. Micromech. Microeng. 2007, 17 (12), N99.*

[28] *X. Pan, J. Wu, Y. Ge, et al., J. Sol-Gel Sci. Technol. 2014, 72 (1), 8.*

[29] *J.D. Mackenzie, E.P. Besche, J. Sol-Gel Sci. Technol. 1998 13, 371.*

[30] *M. Houmard, E.H.M. Nunes, D.C.L. Vasconcelos, et al., Appl. Surf. Sci. 2014, 289, 218.*

[31] *M. Houmard, D.C.L. Vasconcelos, W.L. Vasconcelos, G. Berthomé, J.C. Joud, M. Langlet, Surf. Sci. 2009, 603 (17), 2698.*

Copyright:
DOI: 10.1002/sia.6532;
Andreia Rocha Canella Carneiro,
Fábio Augusto de Souza
Ferreira, Manuel Houmard;
Surface and Interface Analysis;

03

Assessment of Possibilities of Ceramic Biomaterial Fracture Surface Reconstruction Using Laser Confocal Microscopy and Long Working Distance Objective Lenses

Sebastian Stach, Wiktoria Sapota, Zygmunt Wróbel, and Ştefan Ţălu

ABSTRACT

A numerical description of fracture is an essential step in searching for the correlations between specific micromechanisms of decohesion and material characteristics designated with the use of fracture mechanics methods. This issue is critical to search for fundamental relationships between chemical composition, technology, structure, and properties of materials. It often happens that fracture surfaces are well developed, which can significantly hinder or even prevent the measurement and reconstruction of the tested material surface geometry. Herein, comparative measurements of a biomaterial surface were performed using laser confocal microscopy.

INTRODUCTION

Qualitative fractography often provides enough knowledge about material fracture mechanisms and fracture morphology but does not give any information useful for designing of new materials. These deficiencies are compensated by quantitative fractography, which enables the presentation of fractographic analysis quantitatively. Measurement of characteristics on a fracture surface and the use of stereological parameters allow a more thorough assessment of the fracture process. The combination of fractographic observation techniques and geometric parameters obtained with quantitative fractography methods gives a comprehensive picture of the fracture process. [1–3]

A numerical description of fracture is important in the search for the correlation between specific micromechanisms of decohesion and material characteristics designated with the use of fracture mechanics methods. [4–6] In this article, comparative measurements of a biomaterial surface were performed using laser confocal microscopy. To this end, short working distance lenses designed to be used with a focused UV laser beam and long working distance objective lenses were used.

Confocal laser scanning microscopy (CLSM) is an imaging method for material surfaces at the nanometer scale. [7–9] The basic premise of CLSM is to obtain a high-resolution, sharp image of the sample, which is mainly achieved by eliminating images outside the lens's focal plane. [7,10] In a confocal microscope, the signal used for image formation reaches the sample area where it is then reflected. The reflected beam must have a small diameter and a large angle of divergence to get a very high resolution. Owing to this, the signal is focused on the detector aperture in a plane common with the lens focal plane. The signal only reaches the focal plane, and the result is an image of the sample in its cross sections. Then, the images can be saved and combined, giving a three-dimensional image of the entire surface with an increased depth of focus (all image elements are sharp and clear).

Optical microscopy methods are used for surfaces where contact with the surface is unacceptable due to the material sensitivity and specificity. There is characteristic variation in the quality and accuracy of the analysis of surfaces obtained using a laser confocal microscope compared to the analysis obtained using a profilometer due to the nature of the respective probes used in each. [11,12] In profilometry, the large surface area needle makes it impossible to measure the asperities smaller than the probe (**Figure 1**). The laser confocal microscope does not have this deficiency— it can measure an area's roughness at much higher resolution (**Figure 2**).

Figure 1: Course of the analysis performed with the contact method.

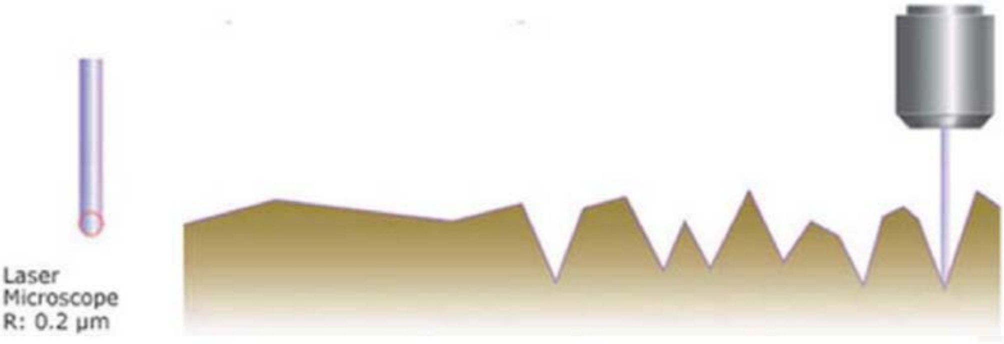

Figure 2: Analysis performed using the CLSM.

METHODS

The study of ceramic surface morphology was performed using the Olympus® LEXT™ OLS4000 laser confocal microscope. The lenses used in the microscope are designed for microscopic tests involving an observation technique in a bright field of view. This technique involves illuminating the sample with a light beam in the form of a cone (previously formed by a condenser) so that all the light covered by the lens apparatus falls on the sample. The obtained contrast results from the differences in light absorption and scattering by different areas of the sample surface. [13]

The Olympus LEXT OLS4000 microscope has a motorized revolving nosepiece that enables an automatic change of the lens during testing. The system automatically adjusts the image sharpness and the light intensity, which allows an easy and quick change of magnification. The lenses mounted in the nosepiece were either semi-apochromatic or apochromatic [14] and ranged from 2.5× to 100×. LEXT dedicated lenses have reduced aberration, which is influenced by a higher numerical aperture and an enhanced optical system, giving a high performance for a 405 nm laser beam. However, they also have a small working distance (1 mm to 0.35 mm); thus, alternative long working distance lenses were also available for surfaces with a high degree of development.

To assess the suitability of long-distance lenses for reconstructing of the geometry of a surface with a relatively high degree of development, it is necessary to carry out comparative studies of short- and long-distance lenses. The test surface cannot be too developed to enable analysis with the lens having the shortest working distance. For comparative studies, an aluminum oxide (Al_2O_3) sample with a relatively flat surface was deposited electrolytically on an aluminum alloy.

RESULTS AND DISCUSSION

To compare the results of analyses obtained using two types of lenses mounted on two different revolving nosepieces, it was neces-

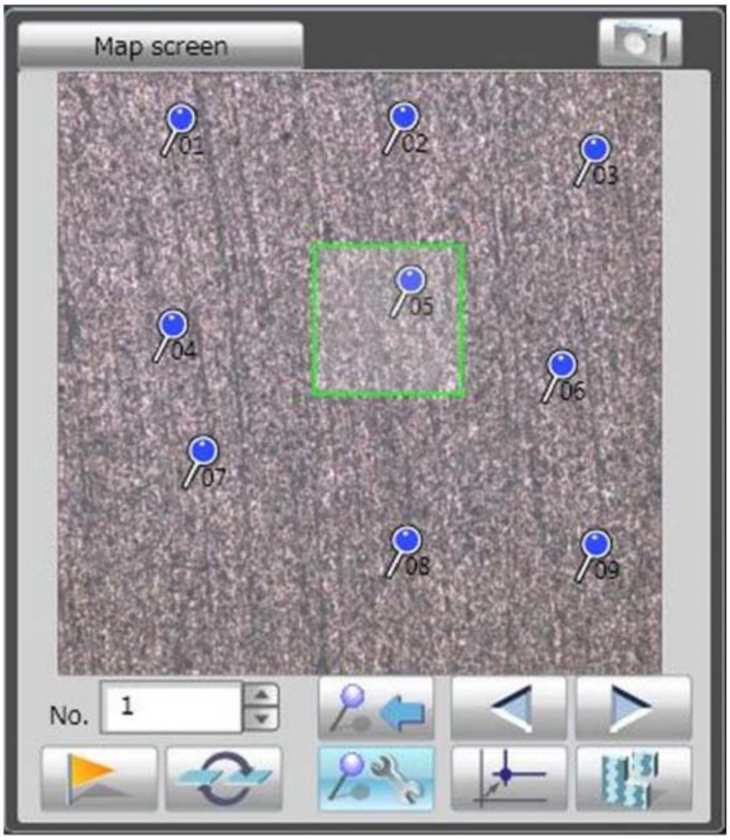

Figure 3: Nine coordinates of the table position defined on the observed surface.

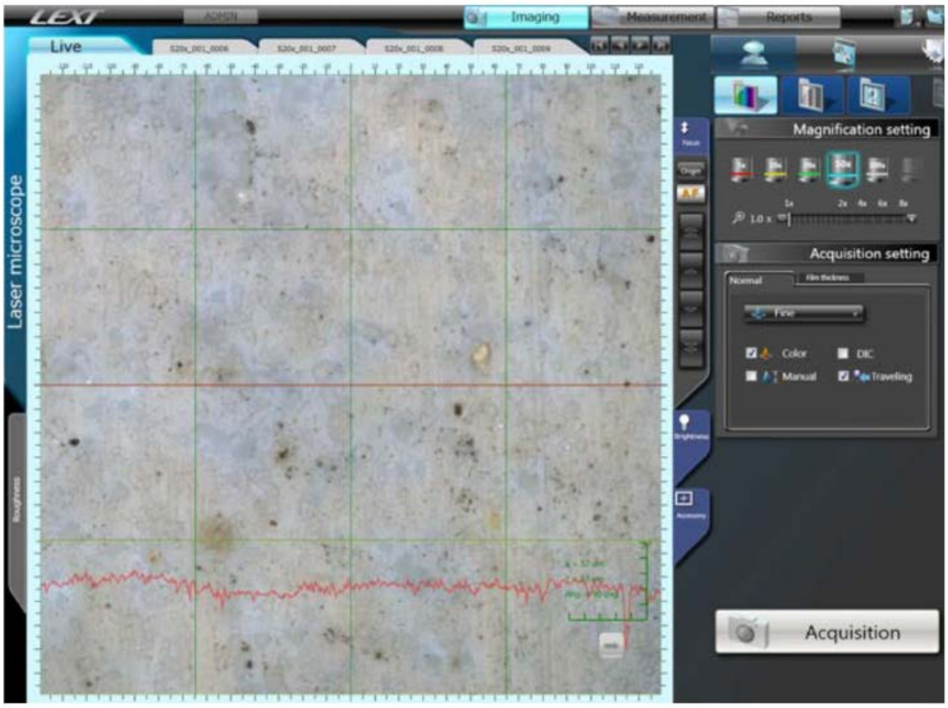

Fine

☑ Color ☐ DIC

☐ Manual ☑ Traveling

Figure 4: Screenshot of the observed surface for the 50× lens.

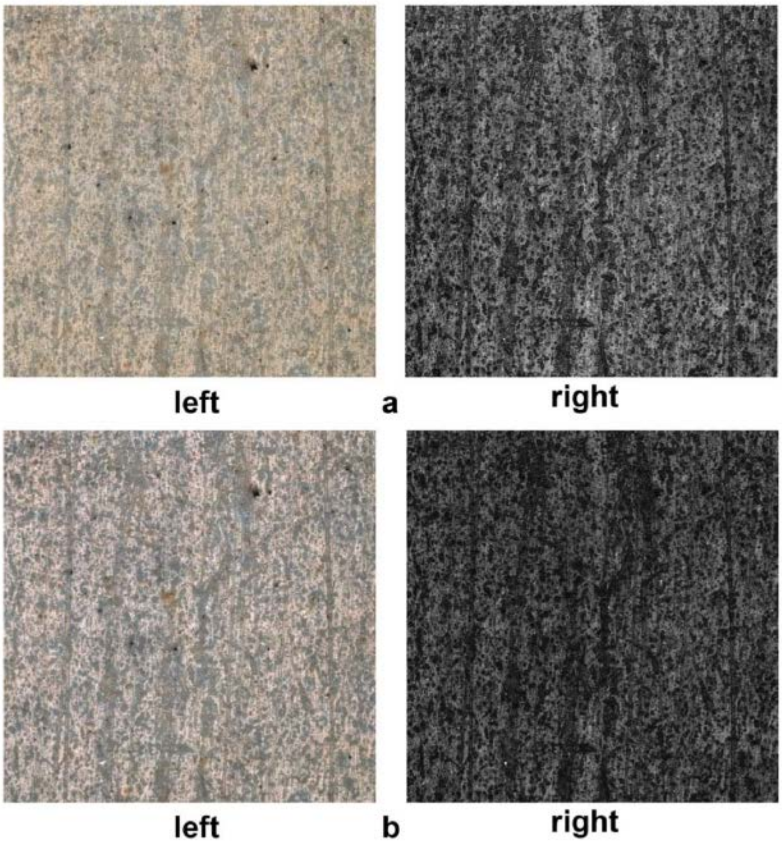

Figure 5: Surface images obtained with 20× lenses. **a:** Short distance. b: Long distance. The first image in the lines was obtained in 2D mode (white light), and the other one in 3D mode (laser light).

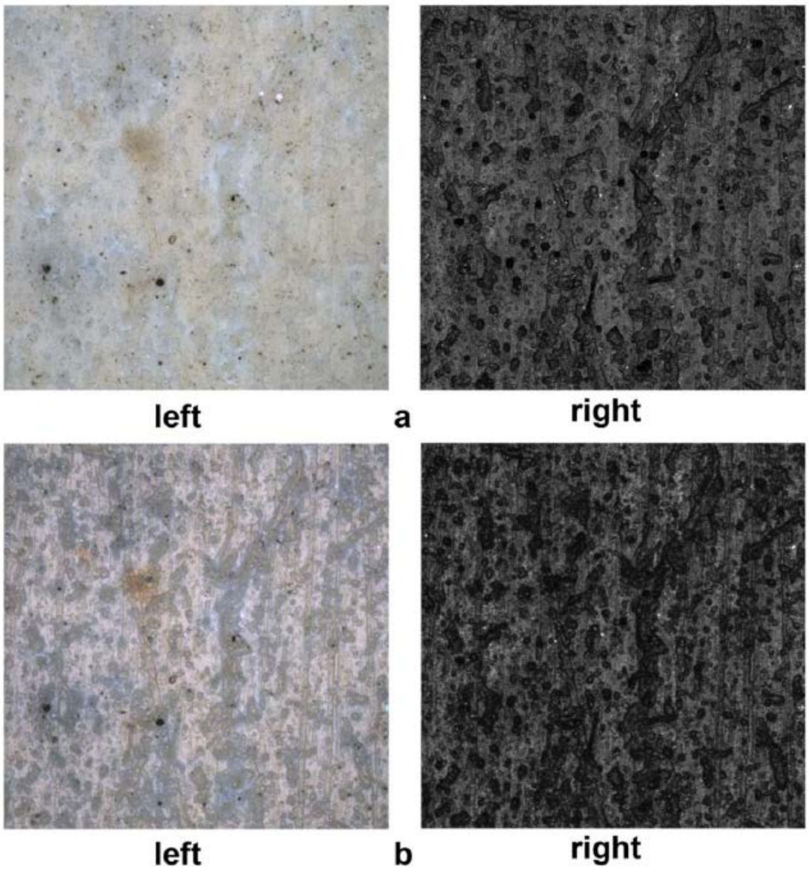

Figure 6: Surface images obtained with 50× lenses. a: Short distance. b: Long distance. The first image in the lines was obtained in 2D mode (white light), and the other one in 3D mode (laser light).

sary to develop a system of analysis, which would enable us to observe precisely the same areas after replacing the revolving nosepieces. For this purpose, the option of stage coordinates available in the microscope software was used, and nine coordinates of the table's position with the sample were defined (**Figure 3**). The observed surface was centered relative to the characteristic place in the observed image, and, additionally, screenshots of the observed area were performed (**Figure 4**).

First, the ceramic coating sample was analyzed in the nine different locations, using the 20× and 50× LEXT lenses with short working distances. The sample was preset using the table coordinates, and then its position was corrected manually by observing the sample with the 50× lens and using previously captured screenshots. This procedure ensured that the observed area was the one that was previously measured.

Second, the sample was observed using 20× and 50× lenses with a larger working distance. It was necessary to calculate the table settings by adjusting the previously set coordinates to repeat the centering of the observed surface using the previously captured screenshots. The results of observation with short-distance and long-distance lenses are given in **Figure 5** and **Figure 6**.

20× lenses enabled observation of the surface sized 639 μm 3 639 μm with a sampling step of 625 nm in the X and Y axes, and 485 pm in the Z-axis. 50× lenses enabled observation of the surface sized 256 μm × 256 μm with a sampling step of 250 nm in the X and Y axes, and 208 pm in the Z-axis. The surface observation was carried out in 2D (white light) and 3D fine (laser light) modes, and the obtained images had a resolution of 1,024 points by 1,024 lines.

For all measurement data, an analysis of the surface morphology was performed (**Figure 7**) using the height parameters,[15] namely Sq, Sp, Sv, Sz, and Sa, where:

Table 1: Results of the surface morphology analysis

		Short distance					Long distance				
Lens	**Area**	**Sq (μm)**	**Sp (μm)**	**Sv (μm)**	**Sz (μm)**	**Sa (μm)**	**Sq (μm)**	**Sp (μm)**	**Sv (μm)**	**Sz (μm)**	**Sa (μm)**
20×	1	1.12	8.44	12.72	21.16	0.78	1.41	10.76	13.18	23.94	1.07
	2	1.16	9.09	11.65	20.74	0.81	1.47	10.74	11.08	21.81	1.12
	3	1.17	9.92	12.09	22.01	0.82	1.47	11.82	12.73	24.56	1.13
	4	1.16	8.38	11.84	20.22	0.81	1.49	7.78	14.16	21.94	1.14
	5	1.08	9.02	11.43	20.45	0.75	1.37	7.51	11.47	18.98	1.05
	6	1.26	10.88	11.5	22.38	0.89	1.53	10.28	12.23	22.51	1.17
	7	1.22	10.11	11.98	22.09	0.87	1.54	7.5	12.12	19.62	1.18
	8	1.11	11.23	11.81	23.04	0.78	1.45	9.99	12.12	22.12	1.12
	9	1.23	8.83	11.7	20.53	0.87	1.47	8.98	13.36	22.34	1.13
50×	1	1.03	4.46	9.95	14.42	0.69	1.18	6.11	10.26	16.37	0.85
	2	1.08	4.53	6.98	11.51	0.74	1.27	4.88	10.14	15.03	0.92
	3	1.11	3.66	9.57	13.23	0.77	1.47	12.66	9.14	21.8	1.01
	4	1.13	3.62	6.86	10.48	0.84	1.32	3.89	10.32	14.2	1.02
	5	0.91	3.49	7.31	10.8	0.63	1.09	5.03	8.41	13.44	0.82
	6	1.17	4.17	10.34	14.5	0.82	1.37	3.97	10.31	14.28	1.02
	7	1.19	5.03	8.63	13.66	0.81	1.36	5.05	11.21	16.26	0.99
	8	1.03	2.75	8.66	11.4	0.74	1.23	3.64	8.02	11.65	0.94
	9	1.04	4.74	9.6	14.35	0.7	1.22	5.98	9.6	15.58	0.9

Sq—Root mean square height is the standard deviation of the height distribution or RMS surface roughness.
Sp—Maximum peak height is the height between the highest peak and the mean plane.
Sv—Maximum pit height is the depth between the mean plane and the deepest valley.
Sz—Maximum height is the height between the highest peak and the deepest valley.
Sa—Arithmetical mean height is the mean surface roughness.

These parameters belong to the height parameters included in ISO 25178-2. [15] Height parameters are a class of surface finish parameters that quantify the Z-axis perpendicular to the surface. The results of the surface morphology analysis are given in **Table 1**.

When analyzing the images (**Figure 5** and **Figure 6**), it can be noticed that the long-distance lenses give a better quality of an image observed in white light than the short-distance dedicated LEXT lenses. The opposite is the case when dimensional images obtained under the illumination of the surface with a focused laser beam are compared. A comparison of the surface morphology analysis (**Table 1**) for 20× lenses shows that relatively higher height parameters were obtained for the long-distance lenses compared with the short-distance ones. The situation is similar when comparing 50× lenses. However, the differences are much smaller than in the case of 20× lenses.

Synak et al. successfully used the Sq parameter to compare roughness measurement results obtained with different methods. Given the large difference in the measurement principle and the large difference in the size of the measured surface areas, which exist in both methods used, [16] the authors concluded that results' compatibility is high. Greater divergence of results occurred in the case of surfaces with Sq less than 2 nm. A large change of this parameter depending on the test area was found when examining such surfaces, which indicates that the heterogeneity of the height of surface roughness may be the leading cause for the measurement differences.

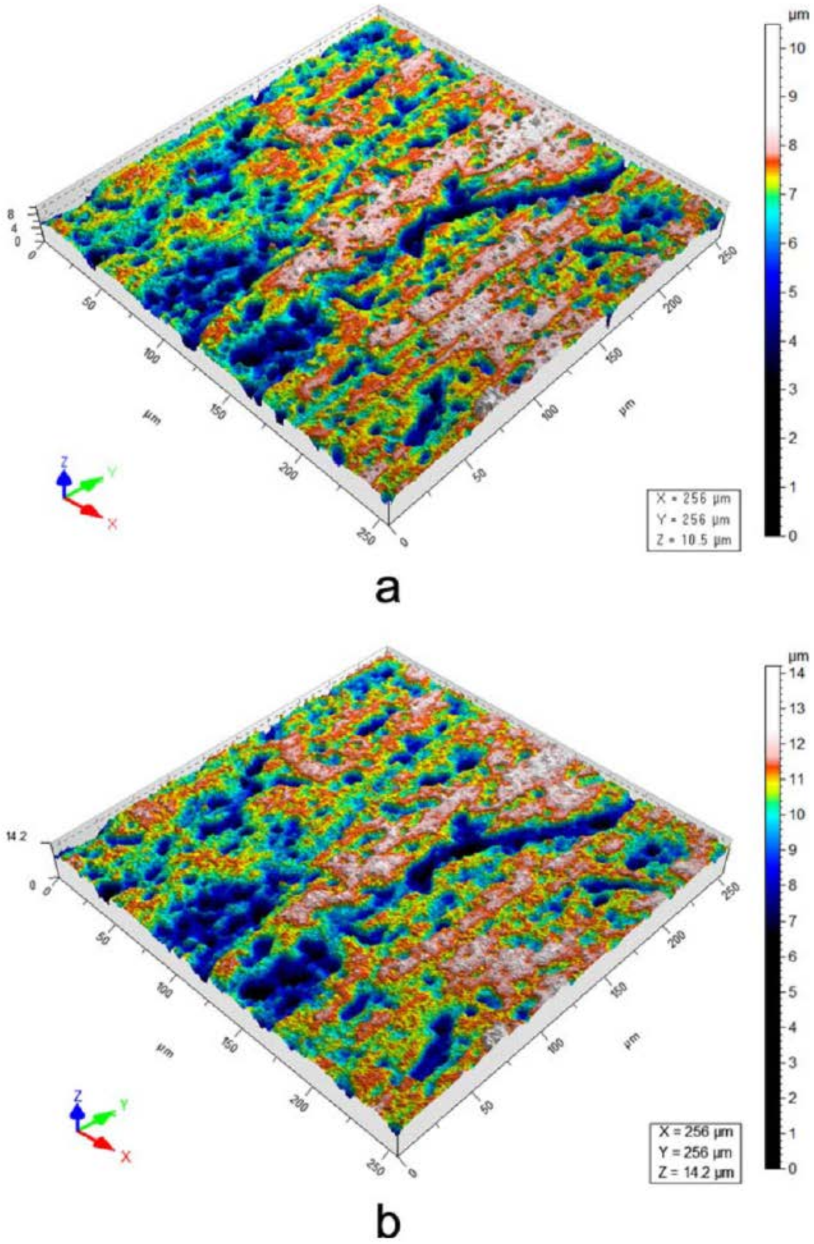

Figure 7: Stereometric view of the sample surface obtained with 50× lenses. **a**: Short distance. **b**: Long distance.

Table 2: RMS calculated for the difference of subtracted surfaces

	Sq (µm) 20×	Sq (µm) 50×
1	1.04	0.6
2	1.05	0.63
3	1.06	0.94
4	1.06	0.63
5	1.04	0.59
6	1.08	0.62
7	1.07	0.63
8	1.07	0.61
9	1.1	0.61

Thus, to emphasize the differences between the surfaces, subtraction of surfaces obtained for both types of lenses was performed. The value of the RMS parameter (Sq, root mean square deviation) of the resulting surface allows verifying the quality of the subtraction. [15] Sq values are given in **Table 2**. The values of RMS are satisfactory and prove that the observed surfaces are very similar.

CONCLUSIONS

To conclude, it was found that an indisputable advantage of confocal microscopes is that they provide images of very high quality and resolution compared to conventional optical microscopy. The sharpness is not only limited to an area or point but the entire image. Bright and clear images result from using a confocal aperture and advanced lenses arranged in front of the detector. Detector signal selection, specialized shapes, and the lenses inside the objective give clear, colorful, and sharp images, which enable the imaging of individual elements of the sample surface. Two-dimensional observations allow the testing and analysis of individual surface layers, whereas three-dimensional observations enable the observation of diverse surface shapes and assess the quality of materials. Lastly, long-distance lenses made it possible to reconstruct the material surface geometry and the description of its morphology.

REFERENCES

[1] *J. Cwajna, S. Roskosz, Mater. Charact. 2001, 46, 183.*

[2] *S.W. Freiman, J.J. Mecholsky, Quantitative Fractography. In: The Facture of Brittle Materials: Testing and Analysis. Hoboken, NJ: Wiley, 2012, pp. 191.*

[3] *G.D. Quinn, Guide to Practice for Fractography of Ceramics and Glasses, NIST Special Publication SP 960–16, 2007, Washington: U.S. Government Printing Office.*

[4] *D.R. Moore, A. Pavan, J.G. Williams, Fracture Mechanics Testing Methods for Polymers, Adhesives and Composites. 2001, ESIS Publication 28. Oxford, UK: Elsevier.*

[5] *S. Stach, Key Eng. Mater. 2011 465, 271.*

[6] *G.D. Quinn, Microsc. Anal. 2008, 22, 21.*

[7] *R.W. Kelsall, I.W. Hamley, M. Geoghegan, Nanotechnologies. Warsaw: Polish Scientific Publishers PWN 2009.*

[8] *S.W. Paddock, Mol. Biotechnol. 2000 16, 127.*

[9] *F. Ren, I.OP Smith, M.J. Baumann, E.D. Case Int. J. of Appl. Ceramic Technol. 2005, 2, 3, 200.*

[10] *W. Brutkowski, Kosmos 2013, 62, 171.*

[11] *M.W. Davidson, M. Abramowitz. Optical Microscopy. In: Encyclopedia of Imaging Science and Technology, 2002, NY: Wiley. pp. 1106–1141.*

[12] *S. Stach, Key Eng. Mater. 2011, 465, 271.*

[13] *"LEXT OLS4000 Industrial Laser Confocal Microscopes - Olympus 3D Laser Measuring Solution." Olympus, 6 May 2011, www.olympus-ims.com/en/metrology/ols4000.*

[14] *"Semi Apochromat Color Correction Brightfield Objective Lenses | LMPLFLN | Olympus." Olympus, 2 May 2011, www.olympus-ims.com/en/microscope/lmplfln.*

[15] *ISO 25178-2, Geometrical Product Specifications (GPS) - Surface texture: Area - Part 2: Terms, definitions and surface texture parameters, Geneva: International Organisation for Standardization, 2012.*

[16] *R. Synak, M. Pawełczak, W. Lipinski, W. Gocman, Electron. (Inform. Technol.) 2013, 54, 46.*

Copyright:
DOI: 10.1002/jemt.22641;
Sebastian Stach, Wiktoria Sapota,
Zygmunt Wróbel, Ştefan Ţălu;
Microscopy Research & Technique;

5 tips for writing better science papers

1

Don’t underestimate the importance of your cover letter

A good cover letter explains to the editor the critical question your research addresses, how you have answered this question, and why it is of significance to the wider community.

2

Keep the title simple: be consistent, not too technical, and concise

It’s important to grab the attention of your editor/reviewer/reader right away and give them an idea of why your paper is a scientific breakthrough. The title also plays into search engine optimization for your article, so think of which search terms you would use when searching for your paper, and try to incorporate those keywords into your title.

3

Don’t cram the abstract with details

What you want is to grab the reader’s attention with the first statement, add a few of the most important details, then leave them with the overall message of the manuscript in the last sentence.

4

Introduce your research with its importance

The reader needs to know the background to your research and, most importantly, why your research is important in this context. What critical questions does your research address? Why should the reader be interested?

5

You might be tempted to share all your war stories… but don’t

When reporting results, keep your focus and make your R&D concise but informative.

Scientific Publishing: The Introduction

P. Trevorrow, G. E. Martin

This article is a short version of the comprehensive and freely available tutorial "How to write a research article for MRC", written by Paul Trevorrow and Gary E. Martin.

IMPORTANT FIRST IMPRESSIONS AFTER THE TITLE AND ABSTRACT

The Introduction should discuss why you did the research and why it is valuable or necessary. This should be complemented by an expert understanding of prior work in this field, typically via a literature review highlighting the significance of your research in the context of the scientific record. The introduction should cover what is known, what is unknown, and the objective of the current study. A useful guide on how to structure one's introduction is offered by Boyd [R. K. Boyd, *Rapid Commun. Mass Spectrom.* 2012, 26, 1725]. While this guidance is offered in respect to the mass spectrometry discipline, it offers an extremely useful system for the structuring of an introduction. In the Boydian method, the introduction should be considered in four parts or subsections. The first three of which provide a "drill-down" from the general to the specific, topped off with a final subsection discussing the objective of the work as a segue into the Experimental section.

Broken down, these sections can be viewed as follows:

- **Subsection 1**

Broad context behind the experiment—include citations of the broader relevant literature here.

- **Subsection 2**

Narrowing down to the specific problem addressed by the research.

- **Subsection 3**

Zeroes in the specific problem, more detailed review of the literature specific to the investigation, with an expert theoretical and experimental critique. Be cautious in this section to keep the literature review relevant, focus on research that is directly relevant to the topic at hand.

- **Subsection 4**

Objective of the present work—this section should simply reflect the main objective of the research as described in the rationale section of the abstract.

THE ANATOMY OF A RESEARCH ARTICLE

Research articles generally follow two standard formats, depending on the nature of the investigation. Although the headings in these structures may be named differently from journal to journal, these formats are commonly referred to as IMRaD and IRDaM. Each of these assemblies consist of an Introduction, Methods, Results, and Discussion although the order and structure of these components differ in each variant.

IMRAD

The IMRaD structure is the most common structure used in scientific writing. This structure is as follows:

- **Introduction**
- **Methods**
- **Results and Discussion**

IRDAM

The IRDaM structure is typically used when a hypothesis is tested without having the experiments planned in advance, a progressive investigative trajectory where the results of one experiment inform which experiment should be undertaken next. These are otherwise known as sequential results. The IRDaM structure is composed as follows:

- **Introduction**
- **Results and Discussion**
- **Methods**

Copyright:
Trevorrow, P, Martin, GE. How to write a research article for MRC . Magn Reson Chem. 2020; 58: 352– 362. https://doi.org/10.1002/mrc.5012